AGU PUBLICATIONS

JGR

Journal of Geophysical Research: Earth Surface

RESEARCH ARTICLE
10.1002/2016JF003891

Key Points:
- Snow avalanches can create catastrophic impulse waves when striking a water basin
- Snow avalanches create waves whose amplitude is smaller by a factor of 2 than the amplitude generated by aerial landslides
- Lower impact velocities and buoyancy forces explain the discrepancies between avalanches and landslides

Supporting Information:
- Supporting Information S1
- Table S1
- Movie S1
- Movie S2
- Movie S3

Correspondence to:
C. Ancey,
christophe.ancey@epfl.ch

Citation:
Zitti, G., C. Ancey, M. Postacchini, and M. Brocchini (2016), Impulse waves generated by snow avalanches: Momentum and energy transfer to a water body, *J. Geophys. Res. Earth Surf.*, *121*, doi:10.1002/2016JF003891.

Received 16 MAR 2016
Accepted 14 NOV 2016
Accepted article online 19 NOV 2016

Impulse waves generated by snow avalanches: Momentum and energy transfer to a water body

Gianluca Zitti[1], Christophe Ancey[2], Matteo Postacchini[1], and Maurizio Brocchini[1,2]

[1]Department of Construction, Civil Engineering, and Architecture, Università Politecnica delle Marche, Ancona, Italy, [2]ENAC/IIC/LHE, Ecole Polytechnique Fédérale de Lausanne, Lausanne, Switzerland

Abstract When a snow avalanche enters a body of water, it creates an impulse wave whose effects may be catastrophic. Assessing the risk posed by such events requires estimates of the wave's features. Empirical equations have been developed for this purpose in the context of landslides and rock avalanches. Despite the density difference between snow and rock, these equations are also used in avalanche protection engineering. We developed a theoretical model which describes the momentum transfers between the particle and water phases of such events. Scaling analysis showed that these momentum transfers were controlled by a number of dimensionless parameters. Approximate solutions could be worked out by aggregating the dimensionless numbers into a single dimensionless group, which then made it possible to reduce the system's degree of freedom. We carried out experiments that mimicked a snow avalanche striking a reservoir. A lightweight granular material was used as a substitute for snow. The setup was devised so as to satisfy the Froude similarity criterion between the real-world and laboratory scenarios. Our experiments in a water channel showed that the numerical solutions underestimated wave amplitude by a factor of 2 on average. We also compared our experimental data with those obtained by Heller and Hager (2010), who used the same relative particle density as in our runs, but at higher slide Froude numbers.

1. Introduction

One of the recent problems to be examined in avalanche protection engineering is related to the impulse waves caused by snow avalanches entering a water basin. High-altitude water reservoirs include basins for supplying mountain resorts with fresh water, reservoirs for producing hydroelectricity, and lakes for manufacturing artificial snow in ski areas. Many natural lakes and man-made reservoirs are located in avalanche risk zones, thus, incidents occasionally occur. In February 1999, an avalanche struck a lake close to the village of Göschenen (Switzerland) and emptied it [*Ammann*, 2000]. The resulting snow–water mixture flowed out as a thick viscous fluid and overtopped a 6 m protection wall, damaging dwellings and killing one person. In March 2006, a reservoir for artificial snow production in Pelvoux (France) was filled by a high-speed, dry-snow avalanche. The mixture of water and snow caused a wet-snow avalanche, which swept through a forest and reached the cross-country ski trails in the valley bottom. Avalanche-induced impulse waves also pose a threat to coastlines in northern Europe (Norway and Iceland) and North America (Alaska and Canada). In Stjernøya (an island in the Altafjord, northern Norway), the Lillebukt mining complex is affected by avalanches sliding down the Nabbaren mountain [*Frauenfelder et al.*, 2014]. In April 2014, the dense core of a powder snow avalanche overtopped a deflection wall and caused moderate damage to buildings, while part of the avalanche entered the fjord, although without creating significant waves. In January 1995, above Súðavík, a fishing village on the west coast of Iceland, a layer of compacted snow, 2–3 m thick, detached from an 800 m wide slope 500 m above sea level. It swept through the village (killing 14 inhabitants) and came to a halt in the fjord, generating a 10 m high wave that damaged harbor structures.

These incidents have prompted national and local authorities to take a closer look at dam safety in mountain areas [*Evette et al.*, 2011]. For large facilities, such as reservoirs for hydroelectricity production, engineers can study impulse wave dynamics using small-scale physical models [*Fuchs et al.*, 2011; *Gabl et al.*, 2015]. For smaller projects, engineers use empirical equations to estimate whether avalanche-generated impulse waves

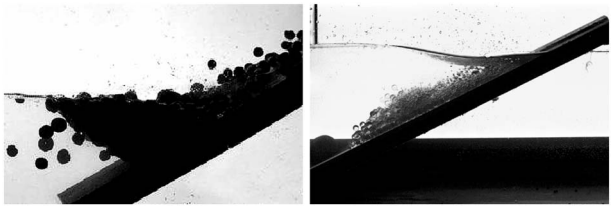

Figure 1. Entry of (left) positively and (right) negatively buoyant particles into water. Once they have penetrated the water, positively buoyant particles come up to the free surface and form clusters that dampen the incoming flow. Conversely, negatively buoyant particles (glass beads) follow the bed and come to a halt on the flume bottom.

put reservoirs and their surroundings at risk [*Heller et al.*, 2009]. These equations have mostly been obtained by extrapolating equations developed for landslides and rock avalanches. For the latter, there is indeed a considerable body of work on impulse waves [*Noda*, 1970; *Kamphuis and Bowering*, 1970; *Slingerland and Voight*, 1979; *Huber*, 1980; *Huber and Hager*, 1997; *Vischer and Hager*, 1998]. Much of the early work to infer the features of impulse waves from landslide characteristics was accomplished experimentally [*Walder et al.*, 2003; *Fritz et al.*, 2003a; *Panizzo et al.*, 2005; *Grilli and Watts*, 2005; *Zweifel et al.*, 2006; *Heller*, 2007; *Di Risio et al.*, 2009; *Mohammed and Fritz*, 2012; *Heller and Spinneken*, 2013]. Over the last two decades, increasing computational power has also made it possible to tackle the formation of impulse waves numerically [*Quecedo and Pastor*, 2004; *Serrano-Pacheco et al.*, 2009; *Kelfoun et al.*, 2010; *Cremonesi et al.*, 2011; *Naaim*, 2013; *James et al.*, 2014; *Crosta et al.*, 2015].

One crucial difference between snow avalanches and landslides is that avalanches involve lightweight bulks (mixtures of air and snow, sometimes with a low content of liquid water and debris). The typical bulk snow avalanche density is 300 kg m^{-3}, which is low compared to densities ranging from 1500 to 2700 kg m^{-3} in landslides and rock avalanches. A direct consequence of this is that once it strikes a reservoir or lake, a landslide mass follows the ground or lake bed and comes to a halt on the bottom, whereas a snow avalanche is prone to float. This fact encouraged us to take a closer look at the problem of impulse waves in the limit of low bulk densities (i.e., when the avalanche involves positively buoyant particles). Preliminary experiments confirmed that there was a significant difference between positively and negatively buoyant particles when entering a body of water, as shown in Figure 1. To get a sense of how important particle buoyancy is in the formation of impulse waves, the reader can examine two videos in the supporting information, from which the close-up snapshots in Figure 1 were extracted.

The present paper focuses on the dynamics of a low-density granular avalanche striking a body of water. More specifically, we are interested in determining how the momentum and energy of the avalanche mass are transferred to the water, producing an *impulse wave* that will propagate away from the point of impact. The classic approach for landslide-generated impulse waves relies on nonlinear, multivariable regression techniques combined with dimensional analysis [*Kamphuis and Bowering*, 1970; *Huber and Hager*, 1997; *Panizzo et al.*, 2005; *Heller and Hager*, 2010; *Mohammed and Fritz*, 2012; *Heller and Hager*, 2014]. An alternative approach has been to use a scaling analysis of the equations of motion, i.e., by recasting the dependent and independent variables in the equations of motion into dimensionless forms [*Walder et al.*, 2003; *Fernández-Nieto et al.*, 2008]. The latter approach is arguably the best, not only to reveal the key dimensionless numbers but also to highlight basic properties such as invariance (e.g., similarity and traveling wave solutions). In the absence of governing equations for modeling the entry of a dilute granular bulk into a body of water, we took a first step toward this by using mixture theory and looking at how momentum is transferred from the particle to the fluid phase (see sections 2 and 3). We ran small-scale experiments, which were based on Froude similarity with snow avalanches (see sections 4 and 5, and Appendix A). Emphasis was given to the earlier stages of avalanche entry into a water body and the ensuing wave's features in two-dimensional geometries. In enclosed basins, waves cannot disperse and are reflected back. As a consequence, the interaction with waves returning to the point of origin could significantly increase the wave amplitudes, the run-up, and the potential for destruction [*Couston et al.*, 2015]. Using a two-dimensional geometry with a smooth topography is a significant simplification of real-world scenarios, which may lead to an overestimation of wave amplitudes under real-world conditions [*Slingerland and Voight*, 1979; *Mohammed and Fritz*, 2012; *Heller and Spinneken*, 2013, 2015]. Analyzing these problems goes far beyond the scope of the present work. An explanatory list of the variables used in this paper is given in the notation section.

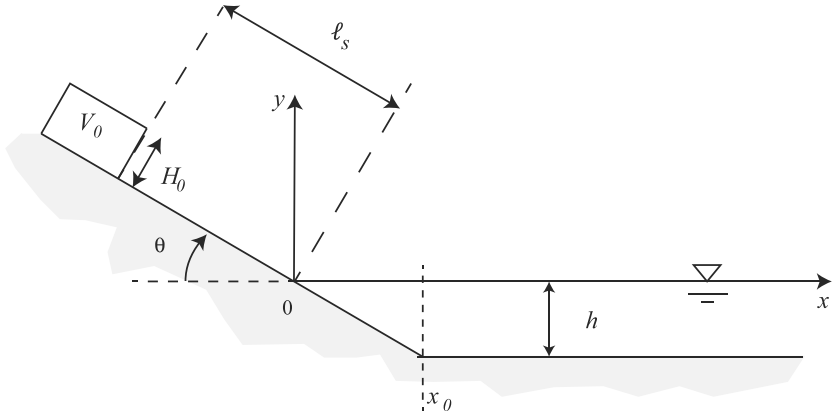

Figure 2. Diagram defining the flow configuration.

2. Theory

2.1. Problem and Notation

We focus on the interaction between a dilute granular avalanche and a two-dimensional body of water (see Figure 2). We consider a granular material composed of solid spherical particles with density ϱ_p and diameter d_p. Here we address the special case of positively buoyant particles, i.e., $\varrho_p < \varrho_f$, where ϱ_f denotes the water density. These particles are initially contained in a box of volume V_0, locked by a gate of height H_0, and fixed to a chute of length ℓ_s and width W. The chute is tilted at an angle θ to the horizontal, and its lower part is immersed in a reservoir whose depth is h and breadth is B. In Figure 2, we have defined a two-dimensional Cartesian coordinate system in which the x axis points down the flume, the y axis is in the direction of the upward pointing normal, and the z axis is the cross-stream direction. The origin of the axes is at the shoreline.

Once the locked gate is opened, particles are free to move down the chute in the form of a dilute granular gas. This flow enters the body of still water. Particles impart their momentum to the water, which starts moving and forming a wave referred to as an *impulse wave*. In the following article, we wish to calculate the main features of this wave.

The impulse wave is generated by the momentum imparted by the granular avalanche. Two main mechanisms are at work: at the particle scale, individual particles carry momentum and as they enter the water, they are slowed down by viscous forces; at a larger scale, the granular avalanche taken as a whole behaves like a continuum. The interface between the immersed part of the avalanche and the rest of the water body is a shock wave $S(t)$ associated with a density jump, as depicted in Figure 3. Ahead of this interface, there is a nonmaterial interface Y, called an acceleration wave [*Chadwick*, 1999] that sets water into motion. Contrary to the frontal shock wave, the velocity and density fields are continuous (only the shear rate experiences a jump across Y). In their measurements based on article image velocimetry, *Fritz et al.* [2003b] and *Zweifel et al.* [2006] provided clear evidence for the existence of these two moving surfaces. As a working assumption, the rest of this paper considers that momentum transfer is mostly achieved through particle-water interactions.

2.2. Conservation of Mass and Momentum

In geophysical fluid dynamics, mixture theory has been routinely used for modeling two-phase flows involving continuous-fluid and disperse-particle phases. Typical examples include submarine avalanches [*Pailha and Pouliquen*, 2009; *Pudasaini*, 2014; *Løvholt et al.*, 2015], saturated granular avalanches [*Berzi and Jenkins*, 2008;

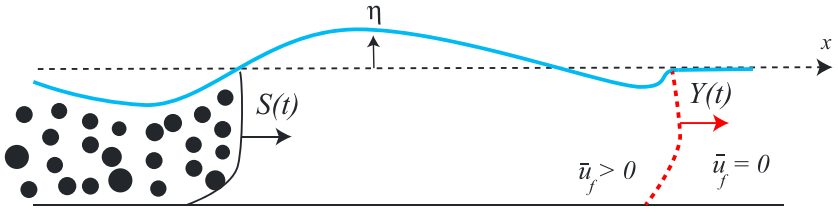

Figure 3. Material interface $S(t)$ and nonmaterial acceleration wave $Y(t)$.

Meruane et al., 2010; *Armanini et al.*, 2014], debris flows [*Iverson*, 2005], suspension transport [*McTigue*, 1981], sheet flow, and bedload transport [*Hsu et al.*, 2004; *Ouriemi et al.*, 2009; *Revil-Baudard and Chauchat*, 2013]. Mixture theory assumes that (i) the mixture of solid particles within a carrier fluid can be treated as a single continuum and (ii) even though the phases are immiscible, any material point is occupied simultaneously by the two phases [*Truesdell*, 1984; *Drew and Passman*, 1999]. The mass and momentum balance equations for each phase are

$$\frac{\partial \alpha_i}{\partial t} + \nabla \cdot (\alpha_i \boldsymbol{u}_i) = 0 \tag{1}$$

$$\alpha_i \varrho_i \left(\frac{\partial \boldsymbol{u}_i}{\partial t} + (\boldsymbol{u}_i \cdot \nabla)\boldsymbol{u}_i \right) = \alpha_i \varrho_i \boldsymbol{g} + \nabla \cdot (\alpha_i \boldsymbol{\sigma}_i) + \boldsymbol{f}_i \tag{2}$$

where the subscript $i = p, f$ refers to the particle or fluid phase, α_i is the fraction of the volume occupied by phase i, $\boldsymbol{u}_i = (u_i, v_i, w_i)$ denotes its velocity, ϱ_i its density, $\boldsymbol{\sigma}_i$ the (total) stress tensor within phase i, $\boldsymbol{f}_i$ the interaction force density between the two phases ($\boldsymbol{f}_p = -\boldsymbol{f}_f$), and $\boldsymbol{g}$ is the gravitational acceleration. In the context of particle flows, it is usual to introduce the solids fraction ϕ, which represents the volume fraction occupied by the particle phase: $\alpha_p = \phi$ and $\alpha_f = 1 - \phi$. For particles suspended in a Newtonian fluid, the interaction force density $\boldsymbol{f}_i$ comprises the buoyancy force $-\phi \nabla p_f$ (where p_f denotes the fluid pressure) and the drag force dependent on the velocity difference $\Delta \boldsymbol{u} = \boldsymbol{u}_p - \boldsymbol{u}_f$ [*Meruane et al.*, 2010]

$$\boldsymbol{f}_p = -\phi \nabla p_f - \pi \varrho_f d_p^2 c \left(Re_\mathrm{p} \right) F(\phi) |\Delta \boldsymbol{u}| \Delta \boldsymbol{u} \tag{3}$$

where c is the drag coefficient, $F(\phi)$ is a correction factor taking particle interactions into account, $Re_p = \varrho_f |\Delta \boldsymbol{u}| d_p / \mu$ is the particle Reynolds number, and μ is the water's dynamic viscosity. For dilute suspensions, the approximation $F(\phi) = \phi$ holds, whereas for concentrated suspensions, $F(\phi)$ is approximated by a power law function in the form $(\phi_c - \phi)^m$, where ϕ_c is the maximum packing concentration and m is a coefficient close to -2. In the limit of high Reynolds numbers, the drag coefficient is close to 0.5. The fluid stress tensor is the Newtonian constitutive equation. For the particle phase, we assume that particles are rigid and that the particle stresses result from the particle interactions (collisions or sustained frictional or lubricated contacts) [*Berzi and Jenkins*, 2008; *Pailha and Pouliquen*, 2009; *Meruane et al.*, 2010; *Armanini et al.*, 2014; *Pudasaini*, 2014]. For the sake of simplicity, we neglect other processes, such as the added-mass effect, particle pressure, interfacial forces, and the pseudo-turbulence due to velocity fluctuations, because their order of magnitude is much lower than the phase interaction force. If the objective were to end up with mathematically well-posed governing equations, it would be essential to take these into account [*Lhuillier et al.*, 2013].

2.3. Integral Form of Mass and Momentum Conservation

Here we used the mass and momentum balance equations in integral form. To do this, we considered a fixed control volume V (see Figure 4). This volume involves three phases: the particles, the water, and the air. Air plays a key part in the early stages of the particles' entry into water [*Truscott et al.*, 2014]: when particles penetrate into the body of water, they entrain ambient air, forming cavities in their wake. These cavities deform, close, and collapse under the action of water pressure and surface tension. Air cavities significantly affect drag forces during water entry [*Truscott et al.*, 2012]. Apart from this influence on water drag a short time after impact, the air contained in V has a negligible role in the dynamics of impulse wave formation, due to its low density. So, in a first approximation, we neglected the air phase.

Initially, the body of water is at rest, and the water pressure is hydrostatic $p_f = \varrho_f g(h - y)$. We assume that pressure remains hydrostatic when the particle phase penetrates into V. Furthermore, we assume that the forces generated by the fluid and particle phases are negligible compared to the momentum fluxes and interaction forces between the phases. We consider that the particle flow remains mostly dilute, and so $F(\phi) = \phi$ (i.e., there are no significant interactions between particles). This is likely to be true in the early stages of water entry, but at later times, particles tend to cluster near the free surface due to their positive buoyancy, which means that the interaction forces between particles become significant compared to the drag forces at later times. It should be kept in mind that by using a standard expression for the drag force, the coupling between the particle and fluid phases has been greatly simplified. Current work on suspensions of large, marginally buoyant particles reveals a complex dynamic, with unexpected features such as turbulence attenuation and greater particle fluctuations [*Cisse et al.*, 2015; *Mathai et al.*, 2015].

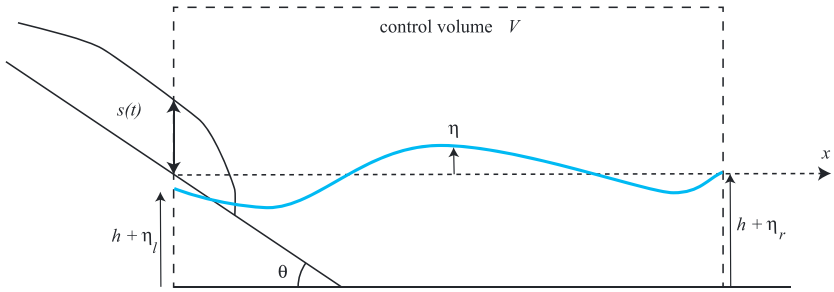

Figure 4. Sketch of the control volume including the shoreline, the impact zone, and part of the water basin.

Across the left boundary of the control volume V, we assume that particles enter V with velocity $\bar{\boldsymbol{u}}_0 = \bar{u}_0$ $(\cos\theta, -\sin\theta, 0)$ and solids fraction ϕ_0. The avalanche height is denoted by $s(t)$ (see Figure 4). The water body's free surface is affected by the entry of particles, and the water depth perturbation is denoted by η_l at this boundary. Across the right boundary, the water flow depth is $h + \eta_r$ and the water velocity is $\boldsymbol{u}_{f,r}$. We assume that the volume V is sufficiently large and the characteristic length of time for wave formation is sufficiently short for the outgoing flow of particles to be negligible.

For each phase, we use the Reynolds transport theorem for the fixed control volume that coincides with the material volume V_m (comprising the fluid and particle phases) at time t [e.g., see *White*, 2011, chapter 3.2]

$$\frac{\mathrm{d}}{\mathrm{d}t}\int_{V_m}\alpha_i\rho_i\mathrm{d}V_m = \frac{\mathrm{d}}{\mathrm{d}t}\int_{V}\alpha_i\rho_i\mathrm{d}V + \int_{S}\alpha_i\rho_i\left(\boldsymbol{u}_i\cdot\boldsymbol{n}\right)\mathrm{d}S = 0 \tag{4}$$

$$\frac{\mathrm{d}}{\mathrm{d}t}\int_{V_m}\alpha_i\rho_i\boldsymbol{u}_i\mathrm{d}V_m = \frac{\mathrm{d}}{\mathrm{d}t}\int_{V}\alpha_i\rho_i\boldsymbol{u}_i\mathrm{d}V + \int_{S}\alpha_i\rho_i\boldsymbol{u}_i\left(\boldsymbol{u}_i\cdot\boldsymbol{n}\right)\mathrm{d}S = \text{forces applied on } V \tag{5}$$

with $i = f, p$. This is the correct way of calculating momentum transfers between moving material volumes.

Mass and momentum balance equations (4) and (5) for each phase can be written in a slightly different manner, which is probably easier to interpret. Let us call $N(t)$ the number of particles within V, $V_f(t)$ the volume of water in the control volume V at time t, and $\varpi_p = \pi d_p^3/6$ the volume of a particle. The volume-averaged particle and fluid velocities are denoted by

$$\bar{\boldsymbol{u}}_p = \frac{1}{V}\int_V \boldsymbol{u}_p\mathrm{d}V \quad \text{and} \quad \bar{\boldsymbol{u}}_f = \frac{1}{V}\int_V \boldsymbol{u}_f\mathrm{d}V \tag{6}$$

Similarly, we define surface-averaged velocities at the control volume boundaries, e.g., for the right boundary, $\bar{\boldsymbol{u}}_{f,r} = S_r^{-1}\int_{S_r}\boldsymbol{u}_{f,r}\mathrm{d}S$, where $S_r = B(h+\eta_r)$ is the surface of the outgoing flow section. The mean square and square mean of any real-valued function X are related to each other through the Boussinesq coefficient $\overline{X^2} = \beta_b\bar{X}^2$. Here, in a first approximation, we set $\beta_b = 1$.

Mass conservation (4) implies that for the particle phase

$$\varrho_p\varpi_p\frac{\mathrm{d}N}{\mathrm{d}t} - \phi_0\varrho_p\bar{u}_0 sB\cos^2\theta = 0 \tag{7}$$

and for the fluid phase

$$\varrho_f\frac{\mathrm{d}V_f}{\mathrm{d}t} + \varrho_f\bar{u}_{f,r}\left(h+\eta_r\right)B = 0 \tag{8}$$

Momentum conservation (5) for the solid phase in the x direction can be cast in the form

$$\varrho_p\varpi_p\frac{\mathrm{d}\left(N u_p\right)}{\mathrm{d}t} - \phi_0\varrho_p\bar{u}_0^2 sB\cos^2\theta = -\pi N c\varrho_f d_p^2|\bar{\boldsymbol{u}}_p - \bar{\boldsymbol{u}}_f|\left(\bar{u}_p - \bar{u}_f\right) \tag{9}$$

with the y projection reducing to

$$\varrho_p \varpi_p \frac{\mathrm{d}\left(N v_p\right)}{\mathrm{d}t} + \phi_0 \varrho_p \bar{u}_0^2 s B \cos\theta \sin\theta = -N\left(\varrho_p - \varrho_f\right)\varpi_p g - \pi N c \varrho_f d_p^2 |\bar{\boldsymbol{u}}_p - \bar{\boldsymbol{u}}_f| \left(\bar{v}_p - \bar{v}_f\right) \tag{10}$$

These equations hold true as long as the particles are immersed. Later on, they approach the free surface and eventually float—a situation that cannot be described by the equations above.

For the water phase, we get

$$\varrho_f \frac{\mathrm{d}\left(V_f \bar{u}_f\right)}{\mathrm{d}t} + \varrho_f \bar{u}_{f,r}^2 \left(h + \eta_r\right) B = \pi N c \varrho_f d_p^2 |\bar{\boldsymbol{u}}_p - \bar{\boldsymbol{u}}_f| \left(\bar{u}_p - \bar{u}_f\right) - \frac{1}{2}\varrho_f g B \left[\left(h + \eta_r\right)^2 - \left(h + \eta_l\right)^2\right] \tag{11}$$

$$\varrho_f \frac{\mathrm{d}\left(V_f \bar{v}_f\right)}{\mathrm{d}t} = \pi N c \varrho_f d_p^2 |\bar{\boldsymbol{u}}_p - \bar{\boldsymbol{u}}_f| \left(\bar{v}_p - \bar{v}_f\right) \tag{12}$$

Equations (7) to (12) form a system of six coupled equations describing the interplay between the particle and fluid phases resulting from an incoming flow of particles. The dependent variables are $\bar{u}_p$, $\bar{v}_p$, $\bar{u}_f$, $\bar{v}_f$, N, and V_f. The momentum balance equation (11) for the water phase is probably the most interesting with regard to the overall dynamics. On its left-hand side, the first term represents the rate of change in the fluid's momentum, whereas the second term reflects the momentum flux across the right boundary of V. The right-hand side reveals that two mechanisms are at play in the momentum change and transfer to the fluid phase: the momentum imparted by the particle phase through the drag force and the pressure force difference.

2.4. Boundary Conditions and Closure Equations

Note that in equations (11) and (12), the flux and pressure terms are evaluated at the left and right ends of the control volume. We assume that at the right end, we have $\bar{v}_{f,r} = 0$. The horizontal velocity component $\bar{u}_{f,r}$ and the free-surface disturbances η_r and η_l are unknown and have to be specified using ad hoc closure equations. For the left boundary, we assume that the difference $\eta_l - \eta_r$ is, on average, zero over time, which is equivalent to implying that the water pressure difference is not a key process in impulse wave generation. Note that experimentally, due to the particle impacts and air cavities, it was impossible to track the water's free surface in the impact zone, and so we were unable to test this working assumption. For the right boundary, analogous to solitary waves generated by a piston wave maker, we assume that the flow depth-averaged velocity is related to the free-surface perturbation [*Guizien and Barthélemy*, 2002]

$$\bar{u}_f = C \frac{\eta}{h + \eta} \tag{13}$$

with $C = \sqrt{g(h + A)}$ the phase speed and A the wave amplitude. As we are primarily interested in an estimate of the wave's features, we further assume that the phase speed at the right boundary is $C = \sqrt{g(h + \eta_r)}$ and the outgoing velocity $\bar{u}_{f,r}$ is close to the volume-averaged velocity, and so we set $\bar{u}_{f,r} = \bar{u}_f$. The closure equation is then

$$\bar{u}_f = \eta \sqrt{\frac{g}{h + \eta}} \tag{14}$$

For the left boundary, the mean particle velocity $\bar{u}_0$, the solids fraction ϕ_0, and the avalanche height $s(t)$ must all be calculated. Several authors have addressed the behavior of a dilute suspension of lightweight particles suddenly released from a reservoir down a sloping bed [*Savage and Hutter*, 1989; *Nishimura et al.*, 1998; *Ancey*, 2001; *Turnbull and McElwaine*, 2008; *Holyoake and McElwaine*, 2012; *Louge et al.*, 2015]. A wide range of behaviors have been reported depending on bottom roughness, bed inclination, particle properties, and initial volume. Here instead of using a theoretical model, we assume that $\bar{u}_0$ and $s(t)$ are prescribed functions that can be determined experimentally. Our experiments showed that velocity $\bar{u}_0$ was not well correlated with avalanche height s, but rather was scaled as $\bar{u}_0 \propto \sqrt{g V_0 \ell_s / \left(W H_0^2\right)}$ (see section 5). Avalanche height $s(t)$ exhibited a fair amount of scatter, but after smoothing the signal, we found that it was bell shaped and could be approximated to a parabolic shape :

$$s(t) = s_{\max}\left(1 - \left(2\frac{t}{T_a} - 1\right)^2\right) \text{ for } 0 \le t \le T_a \tag{15}$$

were $s_{\max}$ was the maximum height and T_a was the avalanche duration at $x = 0$.

2.5. Scaling Analysis

Here we make the governing equations (7) to (12) dimensionless and, in the process, dimensionless groups appear. To make those equations dimensionless, we introduce the following scaled variables

$$t \to T_0 t', \left(u_p, v_p\right) \to \bar{u}_0 \left(u_p', v_p'\right), \left(u_f, v_f\right) \to \sqrt{gh}\left(u_f', v_f'\right), N \to N_0 N', \eta \to h\eta',$$
$$V_f \to Bh^2 V_f', \text{and } s \to s_0 s' \tag{16}$$

where the primed variables are dimensionless, $T_0 = \sqrt{h/g}$ is the timescale, N_0 is the total number of particles (initially contained in the box), and $s_0 = s_{\max}$ is the avalanche height scale. The scaled momentum balance for the particle phase in the x direction becomes

$$\varpi_p \varrho_p N_0 \bar{u}_0 \sqrt{\frac{g}{h}} \frac{\mathrm{d}\left(N' u_p'\right)}{\mathrm{d}t'} - \phi_0 \varrho_p \bar{u}_0^2 s_0 B s' \cos^2\theta = -\pi N_0 N' c\left(\mathrm{Re_p}\right) \varrho_f g h d_p^2 |Fr\bar{\boldsymbol{u}}_p' - \bar{\boldsymbol{u}}_f'| \left(Fr\,\bar{u}_p' - \bar{u}_f'\right) \tag{17}$$

where $Fr = \bar{u}_0/\sqrt{gh}$ denotes the Froude number, often referred to as the *slide Froude number*. A number of dimensionless groups appear when rearranging the terms

$$\Pi_1 = \frac{N_0 \varrho_p \varpi_p}{\varrho_f B h^2}, \Pi_2 = \frac{s_0}{h}, \Pi_3 = \frac{\varrho_p}{\varrho_f}, \Pi_4 = \frac{d_p}{h}, \text{ and } \Pi_5 = \frac{d_p}{B} \tag{18}$$

These dimensionless groups were formed to match the numbers used in previous studies [*Huber and Hager*, 1997; *Heller and Hager*, 2010; *Mohammed and Fritz*, 2012; *Heller and Hager*, 2014] and so facilitate comparison. With this notation, equation (17) becomes

$$Fr\frac{\mathrm{d}\left(N' u_p'\right)}{\mathrm{d}t'} = \phi_0 Fr^2 \frac{\Pi_2\Pi_3}{\Pi_1} s' \cos^2\theta - 6\frac{c\left(\mathrm{Re_p}\right)}{\Pi_3\Pi_4} N' |Fr\,\bar{\boldsymbol{u}}_p' - \bar{\boldsymbol{u}}_f'| \left(Fr\,\bar{u}_p' - \bar{u}_f'\right) \tag{19}$$

whereas in the y direction, we get

$$Fr\frac{\mathrm{d}\left(N' v_p'\right)}{\mathrm{d}t'} = -\frac{1}{2}\phi_0 Fr^2 \frac{\Pi_2\Pi_3}{\Pi_1} s' \sin 2\theta - \left(1 - \frac{1}{\Pi_3}\right) N' - 6\frac{c\left(\mathrm{Re_p}\right)}{\Pi_3\Pi_4} N' |Fr\bar{\boldsymbol{u}}_p' - \bar{\boldsymbol{u}}_f'| \left(Fr\,\bar{v}_p' - \bar{v}_f'\right) \tag{20}$$

For the water phase, we get

$$\frac{\mathrm{d}\left(V_f' \bar{u}_f'\right)}{\mathrm{d}t'} = -\bar{u}_{f,r}'^2\left(1 + \eta_r'\right) + \pi N_0 c \Pi_4 \Pi_5 N' |Fr\bar{\boldsymbol{u}}_p' - \bar{\boldsymbol{u}}_f'| \left(Fr\bar{u}_p' - \bar{u}_f'\right) - \frac{1}{2}\left[\left(1 + \eta_r'\right)^2 - \left(1 + \eta_l'\right)^2\right] \tag{21}$$

$$\frac{\mathrm{d}\left(V_f' \bar{v}_f'\right)}{\mathrm{d}t'} = \pi N_0 c \Pi_4 \Pi_5 N' |Fr\bar{\boldsymbol{u}}_p' - \bar{\boldsymbol{u}}_f'| \left(Fr\,\bar{v}_p' - \bar{v}_f'\right) \tag{22}$$

Mass conservation leads to

$$\frac{\mathrm{d}N'}{\mathrm{d}t'} = \phi_0 Fr \frac{\Pi_2\Pi_3}{\Pi_1} s' \cos^2\theta \tag{23}$$

for the particle phase, and

$$\frac{\mathrm{d}V_f'}{\mathrm{d}t'} = -\bar{u}_{f,r}'\left(1 + \eta_r'\right) \tag{24}$$

for the water phase. Equations (19)–(24) are the governing equations for the scaled variables N', V_f', $\bar{u}_p'$, $\bar{v}_p'$, $\bar{u}_f'$, and $\bar{v}_f'$. They have to be supplemented by three closure equations for $u_{f,r}'$, η_r', and η_l' (see section 2.4):

$$\bar{u}_{f,r}' = \bar{u}_f', \eta_l' = \eta_r', \text{ and } \bar{u}_f' = \eta'\sqrt{\frac{1}{1+\eta'}} \tag{25}$$

Because eight dimensionless numbers have been determined (Re_p, Fr, Π_1 to Π_5, and θ), we deduce that the problem at hand has 8 degrees of freedom. This means that formally, if our intent is to model avalanche-induced impulse waves in the laboratory, we have to explore an eight-dimension parameter space In practice, this is hardly possible. Thus, the next question becomes whether all these dimensionless numbers play a role in the impulse wave's dynamics, and a closely related issue is whether the degrees of freedom can be reduced by leaving aside certain dimensionless groups or by combining some of them. Similar attempts were made by *Heller* [2007] and *Heller and Hager* [2010], who showed that their impulse wave data defined a clear trend when they were plotted as a function of the dimensionless group they called the *impulse product parameter* $\mathcal{P} = Fr\,\Pi_2^{1/2}\Pi_1^{1/4}\cos^{1/2}(6\theta/7)$. This group does not appear explicitly in the dimensionless equations (19)–(24), but we notice that the group $\mathrm{P} = Fr^2\Pi_2/\Pi_1\cos^2\theta$ emerges from the momentum balance equation (19) for the particle phase. The two groups, $\mathcal{P}$ and P, are not identical (among other differences, the exponent of Π_1 differs radically), but their similarity is striking and calls for further analysis. This cannot be done analytically, and in the following section, we will take a closer look at this issue numerically.

3. Numerical Simulations

3.1. Simplified Model

Here, for the sake of simplicity, we provide a proof of concept by considering a simpler model, which is derived from equations (19)–(24) by ignoring the variations in the y direction. As the granular avalanche and water flow mostly in the x direction, this simplification does not introduce significant errors; in particular, it does not modify fluid velocity to any significant degree and the particle velocity is underestimated to within 20%. We provide an example of simulations from the full model in the supporting information.

We solve the following equations numerically:

$$\frac{\mathrm{d}\left(N'u_p'\right)}{\mathrm{d}t'} = \phi_0 Fr\frac{\Pi_2\Pi_3}{\Pi_1}s'\cos^2\theta - \frac{6c}{\Pi_3\Pi_4 Fr}N'\left|Fr\bar{u}_p' - \bar{u}_f'\right|\left(Fr\,\bar{u}_p' - \bar{u}_f'\right) \tag{26}$$

$$\frac{\mathrm{d}\left(V_f'\bar{u}_f'\right)}{\mathrm{d}t'} = -\bar{u}_f'^2\left(1+\eta_r'\right) + \pi N_0 c\Pi_4\Pi_5 N'\left|Fr\bar{u}_p' - \bar{u}_f'\right|\left(Fr\,\bar{u}_p' - \bar{u}_f'\right) \tag{27}$$

$$\frac{\mathrm{d}N'}{\mathrm{d}t'} = \phi_0 Fr\frac{\Pi_2\Pi_3}{\Pi_1}s'\cos^2\theta \tag{28}$$

$$\frac{\mathrm{d}V_f'}{\mathrm{d}t'} = -\bar{u}_f'\left(1+\eta_r'\right) \tag{29}$$

subject to the initial conditions $\bar{u}_p' = 1$, $\bar{u}_f' = 0$, $N' = 0$, and $V_f' = V_{f0}'$ (the initial fluid volume in the control volume), and to the boundary conditions $s'(t') = 1 - \left(2t'/T_a' - 1\right)^2$ for $0 \le t' \le T_a'$ ($s' = 0$ for $t > T_a'$) which is the dimensionless form of equation (15), and $\eta_r' = \frac{1}{2}\left(\bar{u}_f'^2 + \bar{u}_f'\sqrt{4+\bar{u}_f'^2}\right)$ which comes from the wave velocity equation (14). The avalanche duration is imposed by mass conservation: $N' \to 1$ at later times, which imposes setting $T_a' = 3\Pi_1/(2\phi_0 Fr\Pi_2\Pi_3\cos^2\theta)$.

3.2. Example of Simulation

We solved the system of four coupled equations (26)–(29) using the built-in NDSolve function in the Mathematica program. Figure 5 shows a numerical solution for the following specific case: $N_0 = 30,000$ particles and $V_{f0}' = 20$ (see the figure caption for the other parameters).

At first, mean particle velocity decreases, but as the number of particles is increasing at the same time, the momentum of the particle phase $N'\bar{u}_p'$ increases as long as more particles are entering the body of water (see Figure 5a). For times $t' > T_a'$, particle momentum reaches a plateau. Indeed, as the particle velocity quickly matches the mean fluid velocity, the evolution in particle momentum is entirely subject to the fluid velocity. The fluid velocity $\bar{u}_f'$ (not shown here) reaches its maximum at $t' = T_a'$ and then stays constant as flow resistance is zero (due to the assumption of inviscid fluid and zero pressure difference). The closure equation (25) imposes that the wave amplitude η_r' is subject to the fluid velocity and therefore η_r' exhibits the same behavior as $\bar{u}_f'$: the wave amplitude reaches its peak value at $t' = T_a'$, then stays constant (see Figure 5c).

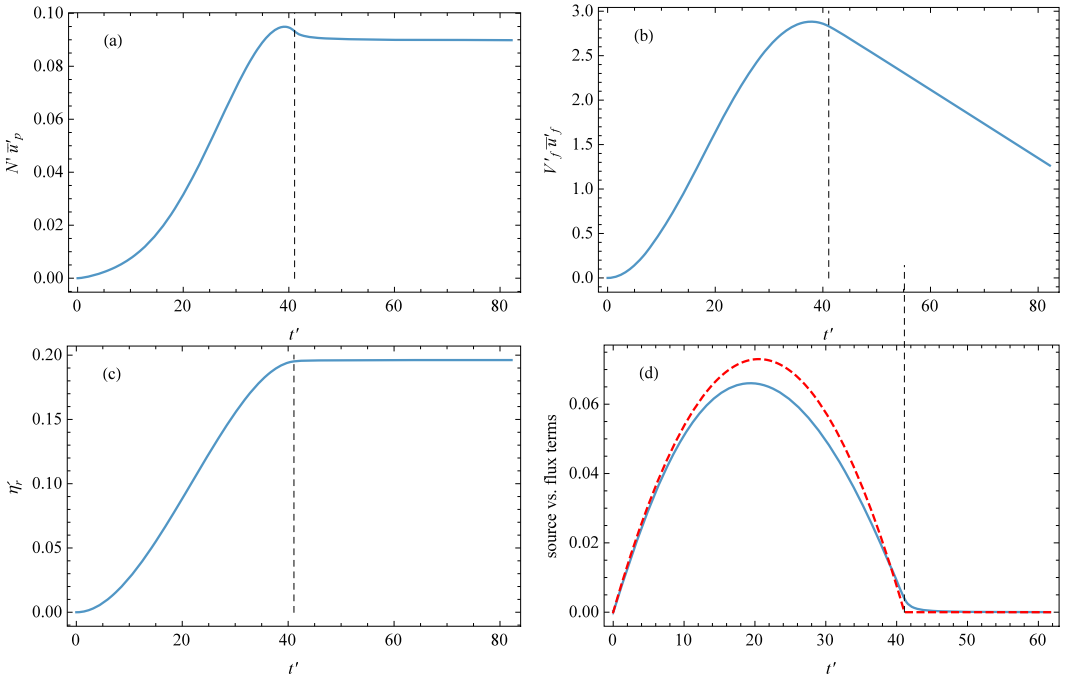

Figure 5. Numerical solution to equations (26)–(29). (a) Time variation of particle momentum $N'\bar{u}'_p$. (b) Time variation of fluid momentum $V'_f\bar{u}'_f$. (c) Time variation of free-surface disturbance η'_r. (d) Time variation of drag force (solid line) $6cN'\left(Fr\,\bar{u}'_p-\bar{u}'_f\right)^2/(\Pi_3\Pi_4)$ and the incoming particle momentum flux (dashed line) $\phi_0 Fr^2\Pi_2\Pi_3 s'\cos^2\theta/\Pi_1$. The dimensionless parameters are $Fr=2$, $\Pi_1=1.5$, $\Pi_2=0.2$, $\Pi_3=0.95$, $\Pi_4=0.05$, $\Pi_5=0.05$, and $\theta=30°$. We assume that $c=0.5$ and $\phi_0=0.2$. The vertical dashed line represents time $T'_a=41.09$, at which the avalanche flux vanishes at $x=0$.

The fluid momentum $V_f\bar{u}'_f$ increases as a result of the momentum transfer from the particle phase; it reaches its maximum at $t'\sim T'_a$ (see Figure 5b) and then decays until there is no longer any water in the control volume. The maximum momentum occurs slightly before T'_a because the fluid volume V_f is a monotonic decreasing function and the product $V_f\bar{u}'_f$ does not reach its maximum at the same time as $\bar{u}'_f$. In the model presented here, there is a rapid momentum transfer from the particle to the fluid phase. As shown in Figure 5d, the drag force matches the changes in the incoming particle flux nearly instantaneously.

3.3. Exploration of the Parameter Space

We explored the parameter space by varying the Froude number and the dimensionless groups Π_1 and Π_2 while keeping the other groups constant. For each run, the free-surface perturbation η'_r was evaluated at time $t'=T'_a$. The initial conditions were $\bar{u}'_p=1$, $\bar{u}'_f=0$, $N'=0$, and $V'_f=50$. The avalanche duration T'_a was fixed by the dimensionless groups $T'_a=3\Pi_1/\left(2\phi_0 Fr\Pi_2\Pi_2\cos^2\theta\right)$.

We then looked for the best correlation between η'_r and a power product of the dimensionless groups $\mathrm{P}=\Pi_1^\alpha\Pi_2^\beta Fr^\gamma$ using various methods (Levenberg-Marquardt nonlinear regression method and Markov Chain Monte Carlo simulations). We found that the numerical data collapsed on the curve $\eta'_r=0.055\mathrm{P}$ when $\alpha=1.074$, $\beta=-0.021$, and $\gamma=1.132$ when $\Pi_3=\varrho_p/\varrho_f=0.95$ (this corresponded to the experiments presented in section 5). This means that η'_r was almost independent of the depth ratio $\Pi_2=s_0/h$ and was almost proportional to the Froude number and the mass ratio Π_1. Figure 6 shows the good agreement between numerical computations and predictions.

We next studied whether other combinations of dimensionless groups were able to capture the numerical trend. When exploring a three-dimensional parameter space, it is difficult to represent the outcome $\eta'_r=\eta'_r(\Pi_1,\Pi_2,Fr)$ graphically. We therefore plotted the smoothed density histograms of the numerical simulations for two combinations of Π_1, Π_2, and Fr. Figure 7a shows how η'_r varies as a function of $Q=\Pi_1 Fr$ for positively buoyant particles ($\Pi_3=0.95$): there is a fairly high correlation between η'_r and Q, with η'_r varying almost linearly with Q ($\eta'_r\sim 0.068Q$). We also tested the impulse product parameter $\mathcal{P}=Fr\,\Pi_2^{1/2}\Pi_1^{1/4}\cos^{1/2}(6\theta/7)$ proposed by *Heller* [2007] and *Heller and Hager* [2010]. Using this dimensionless number led to a fair amount

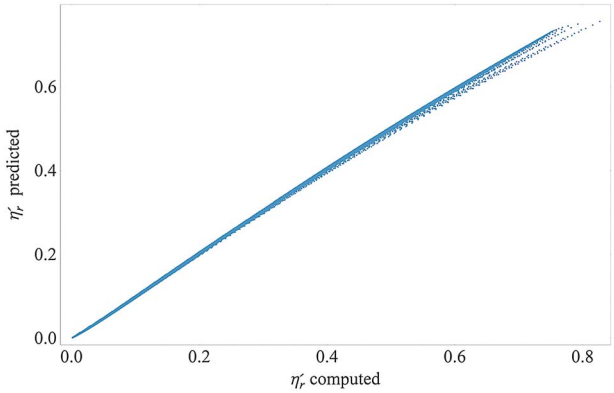

Figure 6. Comparison between the free-surface perturbations computed numerically and those predicted using $\eta'_r = 0.055\mathrm{P}$ with $\mathrm{P} = \Pi_1^{1.07}\Pi_2^{-0.02}Fr^{1.13}$ for $\Pi_3 = 0.95$.

of scatter, and there was far less data (by a factor of 4) than the empirical trend $\eta'_r \sim 4\mathcal{P}^{4/5}/9$ that *Heller and Hager* [2010] fitted to their data.

We also tested the influence of particle density. The density ratio Π_3 was set to 2.7 (corresponding to the relative density of rock), and simulations were run to explore the same parameter space. Again, we sought to express the numerical outcomes as a function of a dimensionless group $\mathrm{P} = \Pi_1^{\alpha}\Pi_2^{\beta}Fr^{\gamma}$. We found that the best fit was $\eta'_r = 0.141\mathrm{P}$ when $\alpha = 1.073$, $\beta = -0.034$, and $\gamma = 1.214$ when $\Pi_3 = \varrho_p/\varrho_f = 2.7$. Again, these coefficients showed little influence of Π_2, and this prompted us to seek a correlation between η'_r and $Q = \Pi_1 Fr$. Figure 8a shows the variations of η'_r with Q. Comparing Figures 7a and 8a, we noticed that η'_r was still well correlated with Q, but the wave amplitude was higher and the empirical trend was nonlinear. In Figure 8a, we plotted both the linear empirical trend $\eta'_r \sim 0.181Q$ and the nonlinear trend $\eta'_r \sim 0.156Q^{1.12}$; the latter performed better at capturing the numerical trend. Interestingly, we noted that the linear trend coefficient depended almost linearly on the density ratio Π_3. So for $0.5 \leq \Pi_3 \leq 3$, we were able to fit the numerical trend using the empirical equation $\eta'_r = 0.07\Pi_3 Q = 0.07Fr\,\Pi_1\,\Pi_3$.

The same exercise was repeated with the impulse product parameter $\mathcal{P}$. Figure 8b shows that the numerical data were more scattered than when using Q (Figure 8a). The same figure also plots the empirical trend $\eta'_r = 4\mathcal{P}^{4/5}/9$ and the variability range given by *Heller and Hager* [2010]. The numerical simulations underestimated Heller's experimental trend by a factor of 2. Both experiments and numerical simulations led to a broad spread of data.

3.4. Summary

In this section, we present a simple model that retains the essential physics of the momentum transfer between a granular avalanche and a body of water. This model is closer to a toy model—one that helps

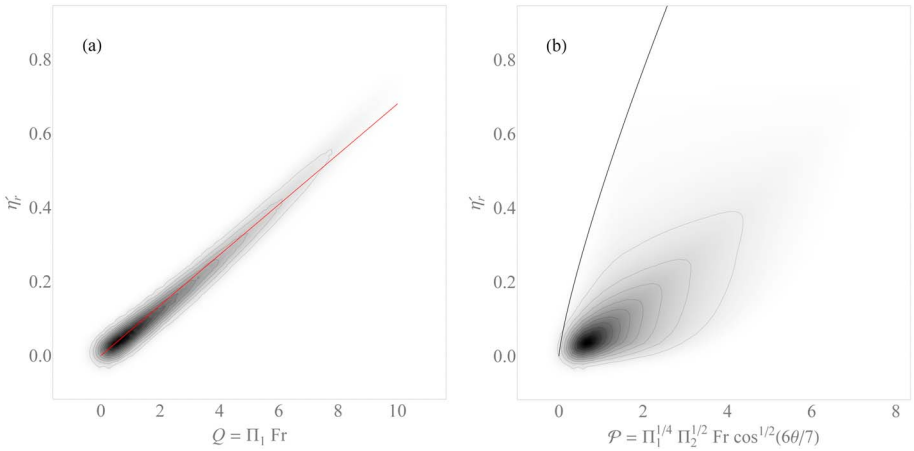

Figure 7. Variation of the free-surface perturbation η'_r using two combinations of the dimensionless groups for positively buoyant particles ($\Pi_3 = 0.95$): (a) $Q = \Pi_1 Fr$ and (b) $\mathcal{P} = \Pi_1^{1/4}\Pi_2^{1/2}Fr\,\cos^{1/2}(6\theta/7)$. In the numerical solutions, Π_1 was varied from 0.05 to 2, Π_2 from 0.1 to 1.5, and Fr from 0.5 to 5. The other groups were kept constant: $\Pi_3 = 0.95$, $\Pi_4 = 0.05$, and $\theta = 30°$. The two plots are smoothed density histograms. The grey shading reflects the level of probability of observing data, and the thin solid lines represent contour lines of equal probability. The straight red line in Figure 7a shows the trend $\eta'_r = 0.068Q$. The thick line in Figure 7b shows Heller's empirical trend $\eta'_r = 4\mathcal{P}^{4/5}/9$. Data smoothing produces false effects near the point of origin, with Q and η'_r taking negative values.

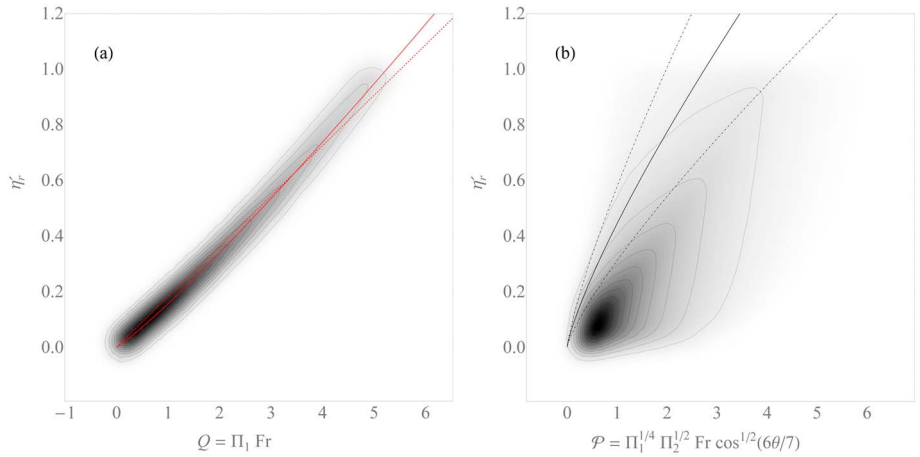

Figure 8. Variation of the free-surface perturbation η_r' with two combinations of dimensionless groups for negatively buoyant particles ($\Pi_3 = 2.7$): (a) $Q = \Pi_1 Fr$ and (b) $\mathcal{P} = \Pi_1^{1/4}\Pi_2^{1/2} Fr \cos^{1/2}(6\theta/7)$. Same caption as for Figure 7. The solid red line in Figure 8a shows the nonlinear approximation $\eta_r' = 0.156Q^{1.12}$, whereas the dashed red straight line shows the linear trend $\eta_r' = 0.181Q$. The thick line in Figure 8b shows Heller's empirical trend $\eta_r' = 4\mathcal{P}^{4/5}/9$, whereas the dash-dotted lines represent the ±30% deviations around the mean trend within which could be found most of the data collected by *Heller and Hager* [2010].

decipher the processes at play in experiments—than to a full model intended to provide realistic predictions of impulse wave formation.

The main result is that the wave amplitude η_r' at the end of the control volume depends on eight dimensionless parameters (Re_p, Fr, Π_1 to Π_5, and θ). Numerical simulations showed that some of the parameters could be aggregated into new dimensionless groups, which reduced the dimension of the problem at hand. Using these assumptions and approximations, we found that η_r' varied proportionally to the group $Fr\,\Pi_1\,\Pi_3$ and showed little dependence on the height ratio $\Pi_2 = s_0/h$. This result is qualitatively in line with the findings of *Heller and Hager* [2010], based on similarity considerations, but whereas the dimensionless group $Fr\,\Pi_1\,\Pi_3$ is similar to Heller's impulse product parameter, the group is not identical. Given the level of approximation and in the absence of a tuning parameter, we find it significant that this simple model is able to predict the wave amplitude in the experiments run by *Heller and Hager* [2010] to within a factor of 2. The next section shows that these simulations also provide correct estimates of the wave amplitude to within a factor of 2 in our experiments.

Altering the values of the free parameters (the drag coefficient c, the mean solids fraction ϕ_0, and the shape function $s(t)$) did not change the numerical results to any significant degree. The effect that the avalanche's bulk density had on wave amplitude was thus almost entirely due to the density ratio $\Pi_3 = \varrho_f/\varrho_p$. This discrepancy between the model and the data will be discussed further in section 6.

4. Experimental Facility

4.1. Setup

The experimental setup aimed to mimic a snow avalanche impact, and, for this purpose, we had to satisfy a number of similarity criteria. These are outlined in Appendix A [*White*, 2011; *Heller*, 2011]. The experimental setup was composed of a wooden chute inclined at an angle $\theta = 30°$ to the horizontal. The upper part was equipped with a lock gate of height H_0, located at a distance ℓ_s from the shoreline (line of contact with the body of water). Its lower part was immersed in a 3 m long flume filled with water. The chute and flume width was $B = 0.11$ m. The flume sidewalls were made of glass; the bottom was composed of an aluminum plate. A light panel was placed parallel to the flume to illuminate the water basin and enhance image contrast. The supporting information includes a photograph of the setup.

The granular material was made of expanded, roughly spherical, clay particles of diameter $d_p = 9$ mm and density $\varrho_p = 955$ kg m^{-3}. Bulk density was measured prior to each mass release, when particles were in the box. Average bulk density was 489 kg m^{-3} (with a standard deviation of 39 kg m^{-3}), meaning that the initial solids fraction was close to 0.51. In the box behind the lock gate, we placed a volume V_0 of granular material

(corresponding to a mass M_0). Initially, the material was wedge shaped for the smallest masses and cuboid shaped for the largest ones. The box length ranged from 2 to 9 cm. The maximum volume released was 1450 mL. Larger volumes were much more difficult to analyze in the light of the theoretical model presented in section 2. Indeed, as particles went up toward the free surface and floated, they clustered and progressively formed a dense layer at that free surface; this dampened the incoming particle flow and affected the momentum transfer between phases.

4.2. Image Processing

Three cameras were placed along the flume, with their optical axis perpendicular to the sidewall. A high-speed camera was located in front of the shoreline to acquire 256 × 785 pixel (px) images of the impact zone at a frequency of 1000 frames per second (fps). This corresponded to a window of either 11.5 × 35.3 cm or 22.8 × 69.9 cm. A square mesh grid was used to undistort the raw images and determine the size conversion factor. Two low-speed cameras were placed along the flume, collecting 120 × 658 px images (corresponding to a window of 22 × 112 cm) of the water's free surface at a frequency of 120 fps. The synchronized images of these two cameras were calibrated and stitched together. The overall length of the observation window was approximately 240 cm (between 230 and 250 cm).

Each experiment was repeated twice. First, water (W) was used to analyze the behavior of the material mass striking the surface and submerged beneath it. Then, colored water (CW) was used to study wave formation and propagation. In W experiments, the focus was essentially on the submerged particles. The high-speed camera was used to measure the input parameters, i.e., avalanche height s, avalanche duration T_a, and particle velocity $\bar{u}_0$. Colored water (CW) experiments made it possible to reconstruct the impulse wave generated by the avalanche impact. The high- and low-speed cameras were used simultaneously to measure the free-surface elevation $h + \eta(x, t)$. The elevation obtained from the high-speed camera was then postprocessed in order to obtain the impulse wave's main characteristics, i.e., its maximum amplitude A_m and maximum height H_m above the observation window. Moreover, the wave energy $E_w(t)$ was estimated from the water surface elevation along the whole flume. Due to the high image acquisition rate and camera resolution, measurement uncertainties were fairly low: for particle velocity, they were less than 2 mms^{-1}, and for wave elevation, they did not exceed 0.8 mm. However, this meant that for some runs with wave amplitudes as low as 5 mm, relative uncertainty reached 20%. Repeatability tests were also carried out, and they showed that wave elevations were reproducible to within 1 px from one run to the other.

5. Experiments

Three different water depths were studied ($h = 0.11$ m, 0.14 m, and 0.18 m) using two chute lengths ($\ell_s = 0.66$ m and 1.21 m). The released mass M_0 varied from 100 g to 700 g using increments of 100 g. Not all of the parameters involved in the theoretical developments were varied in the experiments. We kept ρ_f, ρ_p, d_g, and θ fixed whereas h, M_0, and ℓ_s were varied systematically. This meant that a reduced parameter space of dimension 3 (Π_1, Π_2, Fr) was explored instead of one of dimension 8. The size ratio $\Pi_4 = d_p/h$ took only three values: $\Pi_4 = 0.08$, 0.065, and 0.05. The dimensionless numbers $\theta = 30°$, $\Pi_3 = 0.955$, and $\Pi_5 = 0.065$ were constant. The supporting information recaps the features of the 42 experiments. These data are supplemented with the 71 runs carried out by *Heller and Hager* [2010] with a similar density ratio $\Pi_3 = 0.955$ (but with chute slopes ranging from 30° to 90° and slide Froude numbers in the 0.95–6.8 range).

5.1. Avalanche Features

Image processing was used to determine avalanche height $s(t)$, particle velocity $\bar{u}_0$ at the moment of water entry, the solids fraction ϕ_0, and avalanche duration T_a. As illustrated in Figure 9, the avalanche height s exhibited large fluctuations due to the discrete nature of the particles and the flow shallowness. To smooth out these fluctuations, the parabolic-shape equation (15) was fitted to the $s(t)$ signal. There was a fair agreement between the mean avalanche heights computed by taking the time average $\bar{s}$ of the experimental signal and the parabolic-shape function, which implies that the fit was a good approximation to the measured avalanche height. Image processing (particle tracking) was also used to determine mean particle velocity $\bar{u}_0$. The mean solids fraction was estimated as

$$\phi_0 = \frac{M_0}{\rho_p \bar{s} B \bar{u}_0 T_a} \tag{30}$$

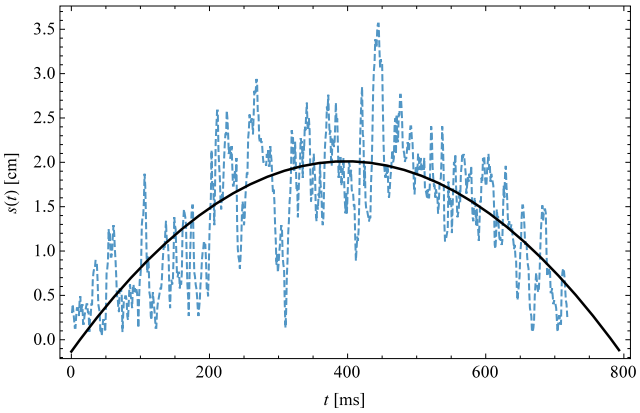

Figure 9. Time variation of avalanche height $s(t)$. The dashed line shows the experimental data, whereas the solid line is the parabolic-shape equation (15) adjusted on the data.

In the example shown in Figure 9, we obtained $T_a = 0.71$ s, $\bar{u}_0 = 1.86$ ms^{-1}, and $\phi_0 = 0.10$. Over all the runs, we obtained $0.46 \leq T_a \leq 2.2$ s, $0.7 \leq \bar{s} \leq 3.3$ cm, $1.11 \leq \bar{u}_0 \leq 2.18$ ms^{-1}, and $0.07 \leq \phi_0 \leq 0.25$ (see the supporting information). Prior to impact, the avalanche's bulk density $\bar{\varrho}_a \approx \phi_0 \varrho_p$ ranged from 67 kg m^{-3} to 240 kg m^{-3}.

We tried to infer how the input variables $\bar{u}_0$ and ϕ_0 were related to the chute geometry (θ, ℓ_s), initial conditions (M_0, V_0, H_0), and flow conditions (s_{max}, T_a). After much trial and error, we found that the mean scaled particle velocity $\hat{u}_0 = \bar{u}_0/\sqrt{gH_0 \cos\theta}$ varied as a power function of the scaled volume $\hat{V}_0 = V_0/(WH_0^2)$, as shown by Figure 10: $\hat{u}_0 \propto \hat{V}_0^p$ with an exponent $p = 0.36$ for $\ell_s = 0.66$ m, and $p = 0.51$ for $\ell_s = 1.21$ m. We failed to find a scaling for ϕ_0, whose actual value depended on many parameters in each run. The avalanches' maximum and time-averaged heights were linked: $s_{max} \sim 2\bar{s}$. In the following, we use the maximum smoothed height $s_0 = s_{max}$ to define the height ratio $\Pi_2 = s_0/h$ in accordance with the definition used by *Heller* [2007]. Owing to the linearity between s_{max} and $\bar{s}$, using the time-averaged $\bar{s}$ does not change the outcomes.

5.2. Wave Features

The wave features for each run were characterized by focusing on two variables: wave amplitude A and height H. Using image processing, we determined the maxima that these variables reached all along the flume (approximately 2.4 m) during each run. The maximum amplitude was observed in the first waves generated by the avalanche.

The following section reports in terms of scaled variables: $A' = A_m/h$ and $H' = H_m/h$. The supporting information also reports the Ursell number $U = H\Lambda^2/h^3$ and wavelength for each run. The Ursell number is used to qualify the degree of nonlinearity of free-surface waves. With $5h < \Lambda < 21h$ and $0.5 < U < 35$, impulse waves could be mostly classified as Stokes or cnoidal waves [*Whitham*, 1974; *Heller and Hager*, 2011].

Determining the maximum wave amplitude from the continuous wave images was straightforward. Impulse waves are nonlinear waves, and, therefore, their height H is usually not equal to $2A$. We defined the maximum wave height H_m as the maximum difference in the wave elevation from trough to crest over the run duration.

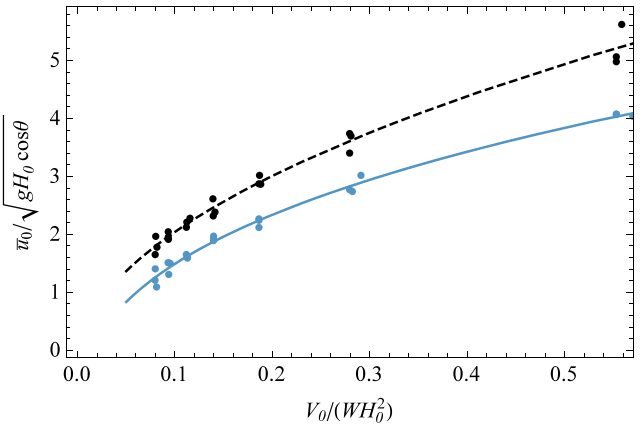

Figure 10. Variation of the scaled particle velocity $\hat{u}_0$ with the scaled initial volume $\hat{V}_0$ for two chute lengths ℓ_s (0.66 and 1.21 m). The solid line shows equation $\hat{u}_0 = -1.4 + 6.82\hat{V}_0^{0.36}$ ($\ell_s = 0.66$ m), whereas the dashed line shows equation $\hat{u}_0 = -0.22 + 7.36\hat{V}_0^{0.51}$ ($\ell_s = 1.21$ m).

Following the procedure used in the numerical simulations in section 3, we sought the best fit for a linear equation $X = \delta P_X$ relating a variable X ($X = A'$ or H') to a dimensionless group aggregating the three numbers Fr, Π_1, and Π_2 in the form of a power product $P_X = \Pi_1^\alpha \Pi_2^\beta Fr^\gamma$. Table 1 reports these results. We now discuss each feature separately. Section 6 addresses the possibility of capturing all experimental trends using a single aggregated dimensionless group.

Figure 11a shows our experimental data, the data collected by *Heller and Hager* [2010] for $\Pi_3 = 0.95$, and the empirical curve $A' = 0.18P_A$. For Heller and Hager's

Table 1. Values of Parameters α, β, γ, and δ Involved in the Nonlinear Regression $X = \delta \Pi_1^{\alpha} \Pi_2^{\beta} Fr^{\gamma}$, As Well As the Coefficient of Determination R^2 for Each Variable

	Amplitude A'	Height H'
α	0.384	0.027
β	0.188	0.365
γ	0.0129	0.667
δ	0.18	0.146
R^2	0.887	0.737

data, the best fit curve was $A' = 0.86P$, and the coefficient of determination was $R^2 = 0.72$. Note that only one of the 71 points from Heller and Hager's data falls within our data: this is the point associated with the lowest P and Fr values, marked with an arrow in Figure 11a. For the other points, a factor of 2 to 4 separates the two data sets. We also tested the empirical equation obtained by *Heller and Hager* [2010]: $A' = 4\mathcal{P}^{4/5}/9$, with $\mathcal{P} = Fr\,\Pi_2^{1/2}\,\Pi_1^{1/4}\cos^{1/2}(6\theta/7)$. This gave a strong coefficient of determination ($R^2 = 0.59$ for Heller's data set), but R^2 was still higher if their equation was recalibrated: with $A' = 0.42\mathcal{P}^{4/5}$, we got $R^2 = 0.81$. Figure 11b shows that equation $A' = 4\mathcal{P}^{4/5}/9$ does equally well at capturing the experimental trend. So a striking feature of this figure is that two radically different definitions of the impulse product parameter (P_A and $\mathcal{P}$) lead to a consistent representation of the wave amplitude, and regardless of the definition of this impulse parameter, there is no match between the two data sets. Finally, the empirical fit determined numerically was tested ($A' = 0.068Q$ with $Q = \Pi_1\,Fr$). Although this equation clearly underestimated the wave amplitude in both experiments by a factor ranging from 2 to 3, on average (the agreement was much better for the highest Q values), it provided the correct order of magnitude.

Figure 12a shows our experimental data, the data collected by *Heller and Hager* [2010], and the empirical curve $H' = 0.146P_H$, for the wave height. As with wave amplitude, we found that our data were a factor of 3 lower than the data gathered by *Heller and Hager* [2010]. The variability was more pronounced for H' than for A', which was reflected in lower coefficients of determination. The spread of the data is more difficult to appreciate in Figure 12b because of the log-log representation. Using $H' = 0.14P_H$, we found that $R^2 = 0.736$; using Heller's empirical equation $H' = 5\mathcal{P}^{4/5}/9$ on his data, we found $R^2 = 0.32$, which was much lower than the value of $R^2 = 0.82$ found by *Heller and Hager* [2010] when they fitted the curve on a larger data set (including runs with $\Pi_3 > 1$, but excluding data affected by scale effects). Figure 12c plots the wave height as a function of P_A. All data lie below the curve $H' = 2A' = 0.36P_A$, which shows that the troughs were slightly less deep than $-A$. On average, we found $H'/A' = 1.45$ (ranging from 1 to 2.5). For Heller's data, we found $H'/A' = 1.26$ on average (ranging from 1 to 1.8).

In summary, the wave amplitudes and heights in our experiments were found, on average, to be a factor of 2 lower than those observed in experiments conducted by *Heller and Hager* [2010] for the same density ratio $\Pi_3 = 0.95$. Comparing our data with the numerical simulations presented in section 3, we also found that the numerical data were off by a factor of 2. Our data did not collapse on a well-defined curve whose equation would highlight a particular combination of the dimensionless numbers Π_3, Π_1, and Fr. When analyzing the respective influence of these numbers on wave features on the basis of the coefficient of determination R^2 (an imperfect measure of the goodness of fit), we found no overall coherent pattern. For instance, the slide Froude number had nearly no influence on wave amplitude (see Table 1), although it significantly affected wave height. More surprising was the fact that we were able to capture the wave features using completely different combinations of Π_3, Π_1, and Fr. Indeed, similarly to what *Heller and Hager* [2010] succeeded in doing with their impulse product parameter $\mathcal{P}$, we were able to fit all the wave features (considered here) using the aggregated dimensionless group $P_A = Fr^{0.0129}\,\Pi_1^{0.384}\,\Pi_2^{0.188}$ (see Figures 11a and 12c).

5.3. Wave Energy

Determining wave energy required significant work. First, let us recall how the energy of free-surface waves is defined. For a fluid slice of height $h + \eta$, depth-averaged velocity $\bar{u}_f$, and infinitesimal thickness dVx, wave energy comprises two terms. The first is the kinetic energy ($\mathrm{d}VE_k = \frac{1}{2}\varrho_f \bar{u_f^2} B(h+\eta)\mathrm{d}Vx$); the second is the potential energy ($\mathrm{d}VE_p = \frac{1}{2}\varrho_f g B \eta^2 \mathrm{d}Vx$). Our experimental setup (see Figure 2) tracked the free surface between the end of the chute ($x_0 = h\cot\theta$) and the right end of the flume ($x_{\mathrm{end}} = 2.24$ m). The wave's potential and kinetic energies in this enlarged control volume are

$$E_p = \frac{1}{2}\varrho_f g B \int_{x_0}^{x_{end}} \eta^2(x,t)\mathrm{d}Vx \text{ and } E_k = \frac{1}{2}\varrho_f B \int_{x_0}^{x_{end}} (h+\eta)\,\bar{u_f^2}\mathrm{d}Vx \tag{31}$$

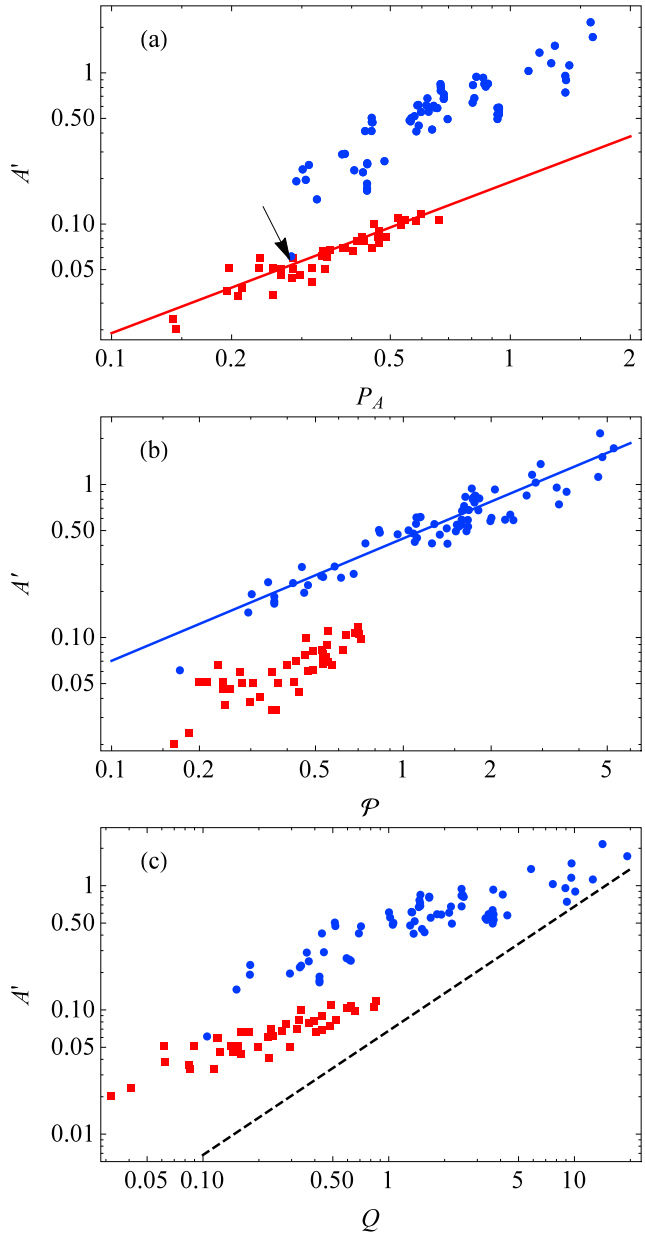

Figure 11. Variation of the maximum-scaled wave amplitude A' with three combinations of dimensionless groups: (a) $P_A = Fr^{0.0129}\,\Pi_1^{0.384}\,\Pi_2^{0.188}$, (b) $\mathcal{P} = Fr\,\Pi_2^{1/2}\Pi_1^{1/4}\cos^{1/2}(6\theta/7)$, and (c) $Q = \Pi_1 Fr$. The graphs show both our data (red squares) and those obtained by *Heller and Hager* [2010] (blue disks). The subplots' straight lines show equations $A' = 0.18P_A$ (Figure 11a), $A' = 4\mathcal{P}^{4/5}/9$ from [*Heller and Hager*, 2010] (Figure 11b), and $A' = 0.068Q$ (Figure 11c). The arrow shows the point where Heller's data came closest to our data set.

Our experiments were unable to track particles and probe fluid velocities at the same time. Thus, to estimate the wave's kinetic energy, we used the closure equation (14) that related $\bar{u}_t$ to η. In doing so, we found that the kinetic energy matched the potential energy: $E_k = E_p$. On average, this result holds true for linear waves and has long been considered a good approximation for impulse waves, in spite of their multimodal shape [*Fritz and Hager*, 2004; *Mohammed and Fritz*, 2012]. Note that *Heller* [2007] obtained quite a different relationship between the kinetic and potential energies. Using particle image velocimetry, he found that $E_k \approx \frac{1}{2}E_p$ in the impact zone. In the absence of further evidence, we consider that the assumption of energy equipartition $E_k = E_p$ provides the upper bound of the wave train's energy.

Figure 13 shows the time variation in the wave train's potential energy E_p for two different chute lengths and flow depths. The potential energy did not show a significant dependence on the chute length: for both of

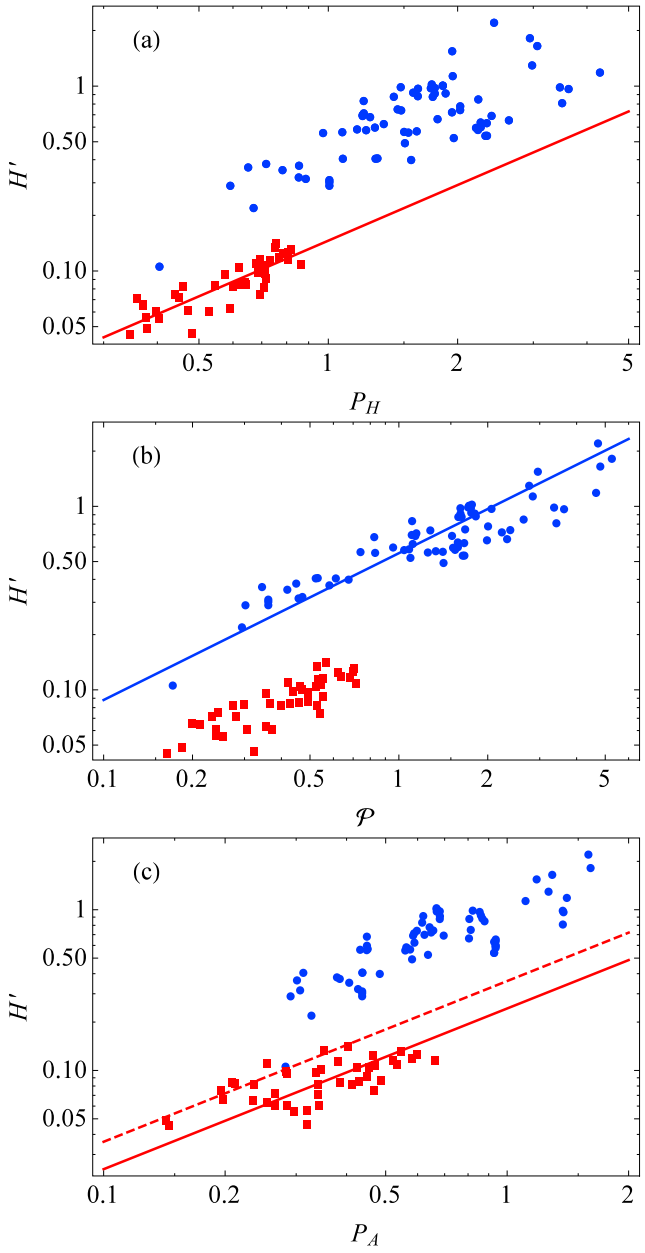

Figure 12. Variation of the maximum-scaled wave height H' with three combinations of dimensionless groups: (a) $P_H = Fr^{0.67}\,\Pi_1^{0.02}\Pi_2^{-0.36}$, (b) $\mathcal{P} = Fr\,\Pi_2^{1/2}\Pi_1^{1/4}\cos^{1/2}(6\theta/7)$, and (c) $P_A = Fr^{0.0129}\,\Pi_1^{0.384}\,\Pi_2^{0.188}$. Graphs show both our data (red squares) and those obtained by *Heller and Hager* [2010] (blue disks). The straight line shows the best fit curve $H' = 0.14P_H$ in Figure 12a, the empirical equation $H' = 5\mathcal{P}^{4/5}/9$ obtained by *Heller and Hager* [2010] in Figure 12b, and the equation $H' = 0.243P_A$ in Figure 12c. In Figure 12c, the dashed line shows the height equation $H' = 2A' = 0.36P_A$ for linear waves.

the flow depths shown in this figure, the evolution of $E_p(t)$ followed the same pattern, independently of the chute length. However, since the mean particle velocity on impact $\bar{u}_0$ was dependent on chute length ℓ_s (see Figure 10), this meant that potential energy was mainly dependent on the mass of the granular avalanche. The curves $E_p(t)$ were remarkably close to each other for times longer than 200 ms. When looking at the avalanche mass's effect on the wave pattern, no predominant pattern could be seen with the naked eye. Nevertheless, by looking at the autocorrelation function $\rho(t)$ of the E_p signal, we observed that these functions were quite similar for a given flow depth h, as shown in Figure 14. If we defined the autocorrelation time t_c as the time when the autocorrelation vanished, then we found that $t_c \sim 0.1$ s for $h = 11$ cm, $t_c \sim 0.3$ s for $h = 14$ cm, and

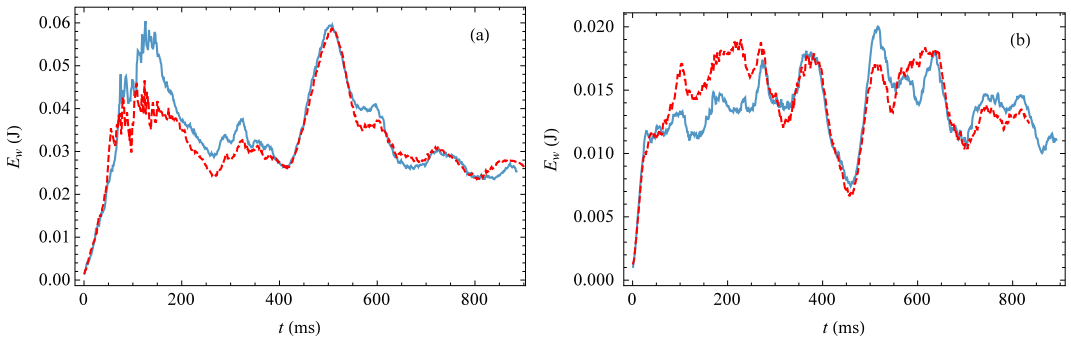

Figure 13. Time variation of the wave's potential energy for (a) $h=11$ cm and (b) $h=18$ cm. The solid line corresponds to the shortest chute length $\ell_s=66$ cm, while the dashed line shows chute length $\ell_s=121$ cm. The initial particle mass was $M_0=700$ g.

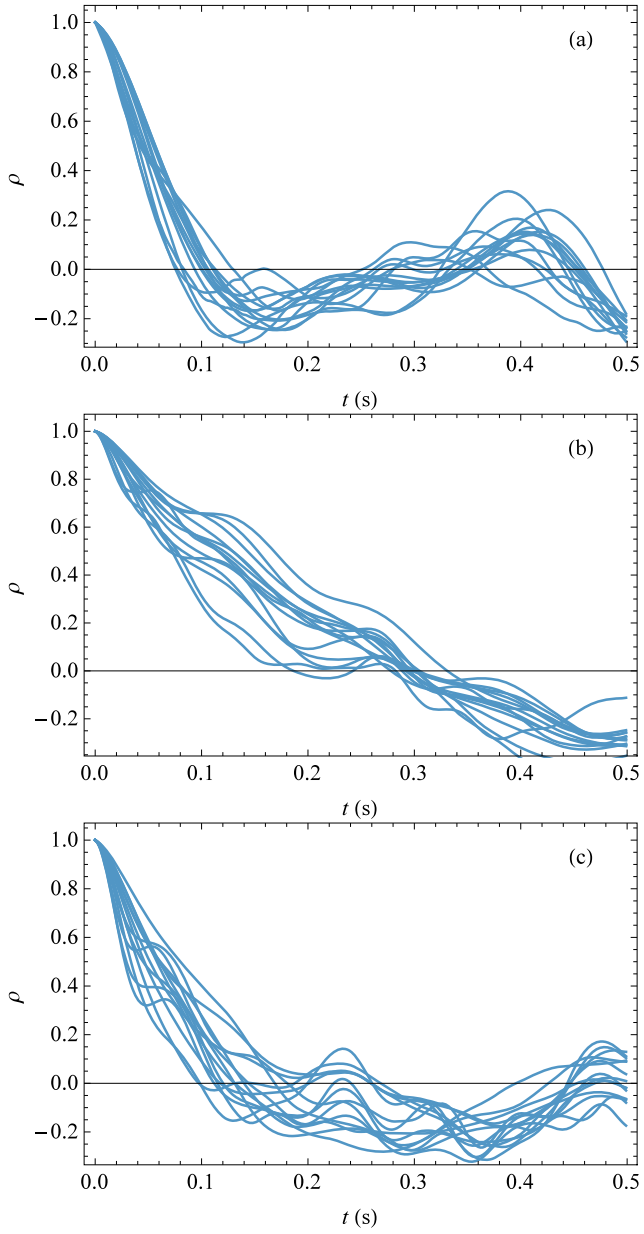

Figure 14. Autocorrelation function of the wave's potential energy for (a) $h=11$ cm, (b) $h=14$ cm, and (c) $h=18$ cm. All runs are reported.

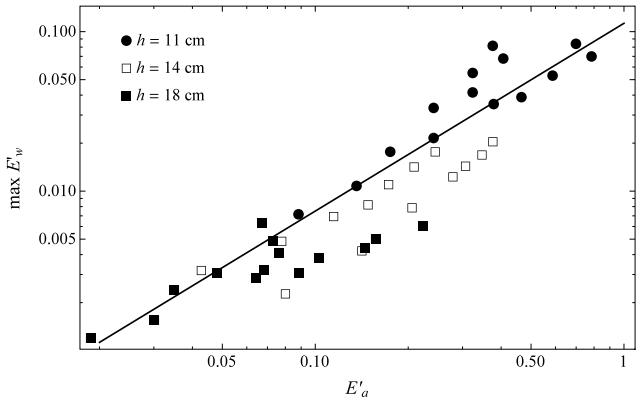

Figure 15. Variation in the wave's energy E'_w in relation to the avalanche's kinetic energy E'_a. The straight line shows the empirical trend $\max E'_w = 0.11E'^{1.178}_a$ fitted to the entire data set.

$t_c \sim 0.15$ s for $h = 18$ cm. Note that the autocorrelation time first increased when h was increased from 11 cm to 14 cm, then decreased when h was increased to 18 cm.

We wished to compare the wave energy with the energy of the avalanche upon impact:

$$E_a = \frac{1}{2}M_0\bar{u_0^2} \tag{32}$$

Figure 15 shows how the wave energy $E_w \approx 2E_p$ varied with the avalanche's kinetic energy. Here we report only the maximum value reached by the wave train. We also plot the experimental trend fitted to our data: $\max E'_w = 0.11E'^{1.178}_a$ ($R^2 = 0.74$). Energies were scaled by $\rho_f g B h^3$. As expected, wave energy varied almost linearly with the avalanche's kinetic energy. The highest energy conversion factor $f_{max} = \max E'_w/E'_a$ occurred with the shallowest reservoirs. For $h = 11$ cm, f_{max} ranged from 0.07 to 0.21. Increasing the flow depth h caused a decrease in f_{max}. For $h = 18$ cm, f_{max} ranged from 0.026 to 0.067. This analysis could have been done using time-averaged wave energy $\langle E_p \rangle$, but this would have not changed the outcome significantly since $\max E_p \approx 1.9\langle E_p \rangle$ (with a standard deviation of 0.21).

6. Discussion

6.1. Lower and Upper Bounds of Wave Features

A large body of work has been devoted to the formation of landslide-induced impulse waves. Most small-scale experiments were carried out using negatively buoyant particles (with a density ratio Π_3 in the 2–3 range). Occasionally, positively buoyant particles have been used [*Zweifel et al.*, 2006; *Heller and Hager*, 2010]. As shown in section 5, we observed a significant difference between our experimental data and those obtained by *Heller and Hager* [2010]: in our experiments, wave amplitudes and heights were, on average, a factor of 2 lower than those observed in experiments conducted by *Heller and Hager* [2010], for the same density ratio $\Pi_3 = 0.95$. We can put forward two possible explanations for this discrepancy.

The first is related to scale effects: physical models based on particles with a small-scale factor λ are more prone to scale effects than models based on a larger scale factor. These effects arise mostly from surface tension and fluid viscosity. *Heller et al.* [2008] showed that when water depth was shallower than 20 cm, scale effects caused a decrease in wave amplitude. As we ran experiments with $h < 20$ cm, one might suspect that this was the cause of the discrepancies observed. Yet if this were the case, we should have observed a gradual transition in the scaled wave amplitude A' from the deepest to the shallowest flows, and this was not the case. Moreover, we took special care to avoid the occurrence of surface tension effects by working at sufficiently high Weber numbers (see Appendix A). We note that *Heller et al.* [2008] studied high-speed granular flows, producing high–slide Froude numbers (in the 0.95–6.8 range, with a mean close to 3.4). In our setup, slide Froude numbers Fr ranged from 1.1–2.1, with a mean close to 1.7. In Figure 11, there was only one point from Heller's experiments that came close to our data set, and it was associated with the lowest Froude number ($Fr = 0.95$). In the end, we cannot exclude that our data were affected, to some extent, by scale effects. Neither can we exclude that the scale limits suggested by *Heller et al.* [2008] hold for low Froude numbers (i.e., for $Fr < 2$).

Another explanation is that impulse waves arise from different initiation mechanisms, which can be distinguished according to the slide Froude number. *Zweifel et al.* [2006] found that for $\Pi_3 < 1$, buoyancy forces only played a key role in the momentum transfer between the particle and fluid phases when $Fr < 2$. *Fritz et al.* [2003b] provided evidence that when high-speed flows disturb a body of water, they produce a hydrodynamic impact crater in it whose collapse causes the impulse wave, provided that the Froude number exceeds a critical value Fr_c, whose value at $\theta = 45°$ is

$$Fr > Fr_c(\theta) = \frac{5}{3} + \frac{1}{2}\Pi_2 \tag{33}$$

Table 2. Lower and Upper Bounds for the Maximum-Scaled Wave Amplitude and Height[a]

		Scaled Amplitude A'	Scaled Height H'
With $\mathcal{R}$	Lower bound	$A' = 0.188\mathcal{R}$ ($R^2 = 0.885$)	$H' = 0.243\mathcal{R}$ ($R^2 = 0.102$)
	Upper bound	$A' = 0.886\mathcal{R}$ ($R^2 = 0.732$)	$H' = 1.00\mathcal{R}$ ($R^2 = 0.628$)
With $\mathcal{P}$	Lower bound	$A' = 0.143\mathcal{P}$ ($R^2 = 0.685$)	$H' = 0.19\mathcal{P}$ ($R^2 = 0.526$)
	Upper bound	$A' = 0.427\mathcal{P}^{4/5}$ ($R^2 = 0.814$)	$H' = 0.48\mathcal{P}^{4/5}$ ($R^2 = 0.483$)

[a]The coefficient of determination R^2 is also reported. Two aggregated dimensionless numbers are used in the equations: $\mathcal{R} = \Pi_1^{0.4}\Pi_2^{0.2}$ and $\mathcal{P} = Fr\,\Pi_2^{1/2}\Pi_1^{1/4}\cos^{1/2}(6\theta/7)$. The lower bound has been fitted to our data; the upper bound has been derived from the selected set of data collected by *Heller and Hager* [2010], for which $\Pi_3 = 0.95$. Also, see Figures 11 and 12 for how these equations compare with data.

For $Fr < Fr_c(\theta)$, impulse waves result from the displacement of the body of water, pushed by the incoming flow. As discussed in Appendix A, our setup was devised so as to create flow conditions with $Fr < 2$, thus mostly satisfying $Fr < Fr_c(\theta)$.

One tentative conclusion from the comparison between our data and those obtained by *Heller and Hager* [2010] highlights the influence of the slide Froude number on impulse wave features (amplitude and height): for low- and intermediate-speed flows with $Fr < Fr_c$, our data would provide the lower bound of these wave features, while for high-speed flows ($Fr > Fr_c$), the relations obtained by *Heller and Hager* [2010] would provide the upper bound. Table 2 recaps the different expressions that can be used for estimating these wave features in engineering applications (for two-dimensional configurations). Wave amplitude and height are expressed as functions of $\mathcal{R} = \Pi_1^{0.4}\Pi_2^{0.2}$ (a simplified variant of $P_A = Fr^{0.0129}\,\Pi_1^{0.384}\,\Pi_2^{0.188}$) and $\mathcal{P} = Fr\,\Pi_2^{1/2}\Pi_1^{1/4}\cos^{1/2}(6\theta/7)$. We also recalibrated the original equations proposed by *Heller and Hager* [2010], since we only considered positively buoyant particles. If we apply their original equations and compute the coefficient of determination R^2 using the data selected, we obtain lower R^2 values. For instance, for the wave amplitude, *Heller and Hager* [2010] obtained $A' = 4\mathcal{P}^{4/5}/9$ and $R^2 = 0.88$ for the whole data set, but we found $R^2 = 0.60$ when applying this equation to the selected data $\Pi_3 < 1$.

6.2. Aggregated Dimensionless Groups

Another striking feature of our work concerns the possibility of expressing the wave features as a function of aggregated dimensionless groups. In section 2, the theoretical model based on mixture theory demonstrated that the wave amplitude A' depended on eight dimensionless parameters (Re_p, Fr, Π_1 to Π_5, and θ). In section 3, numerical simulations confirmed the possibility of reducing the dimension of the parameter space by aggregating the slide Froude number, the mass ratio Π_1, and the density ratio Π_3 into a new dimensionless number $P = \Pi_1\Pi_3 Fr$. The height ratio $\Pi_2 = s_0/h$ had little influence on A', and the other numbers Re_p and Π_5 were not expected to play a significant role either. This made it possible to seek approximate solutions in the form $A' = A'(P, \theta)$. In other words, the dimension of the parameter space dropped from 8 to 2. This substantiates a long-standing practice in the development of empirical equations for predicting impulse waves [*Huber and Hager*, 1997; *Vischer and Hager*, 1998; *Zweifel et al.*, 2006; *Heller and Hager*, 2010, 2014]. Yet experiments told us a slightly different story. First, when we tried to rescale our data using the dimensionless group $Q = \Pi_1 Fr$ (see Figure 11c), the match between the data and the theoretical trend was roughly correct, but far poorer than the empirical fits derived using nonlinear regression techniques. Second, data exhibited a fair amount of scatter, and so there was no unique solution: we could capture the experimental trend using dimensionless product numbers as diverse as $\mathcal{P} = Fr\,\Pi_1^{1/4}\,\Pi_2^{1/2}\cos^{1/2}(6\theta/7)$ (used in particular in *Heller and Hager* [2010, 2014] and *Heller and Spinneken* [2013]), and $\mathcal{R} = \Pi_1^{0.4}\,\Pi_2^{0.2}$ (see Table 2).

6.3. Mechanisms of Momentum Transfer

In section 2, we presented a simple model based on mixture theory, which described the evolution of the momentum transfer between the water and particle phases. This model not only set the stage for the subsequent dimensional analysis of impulse wave formation but also shed light on the key processes driving impulse wave formation. The mismatch between the numerical results and experimental data (see Figure 11c) may be seen as a failure of the model, but, in fact, it reveals something interesting about impulse wave formation. The model systematically underestimated wave amplitude at low Q values, and its poor performance at estimating wave amplitude can be interpreted in two different ways.

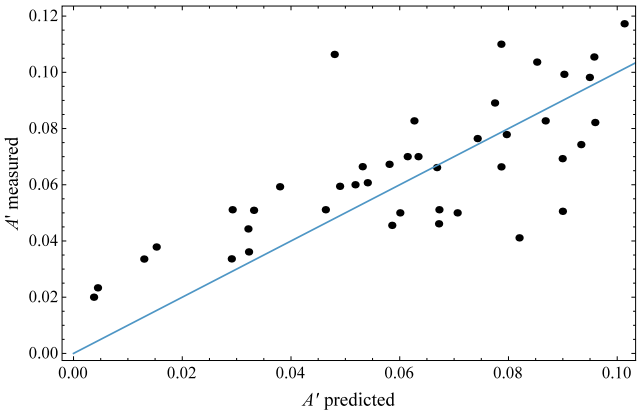

Figure 16. Comparison between our experimental data and the values predicted by equation (34). The straight line is the line of perfect fit.

First, there could be a flaw in how the model was built or how the interaction forces were parameterized. However, this argument does not explain why the model performed much better at high Q values (remember, this model had no tuning parameter).

Second, looking again at the assumptions underpinning our model, we recall that the model emphasized momentum exchanges between the two phases but neglected two key ingredients in the physics of wave formation: the material interface $S(t)$ separating the granular mixture and the water body, and the (nonmaterial) acceleration wave $Y(t)$ (see Figure 3). This neglect was inevitable insofar as we used a control volume to calculate the mass and momentum exchanges. For negatively buoyant particles ($\Pi_3 > 1$) and slide Froude numbers in excess of Fr_c, *Fritz et al.* [2003b] showed that there was a significant uplift of water in the impact zone caused by the avalanche entry and that there was no mixing between the incoming particle flux and the water (these authors referred to this as flow separation). In that case, momentum transfer did not occur on the particle scale but mostly across the interface $S(t)$.

Contrary to linear free-surface waves, acceleration waves carry mass and momentum [*Chadwick*, 1999]. The computation of their features is beyond the scope of this paper, but we can speculate that at low Q numbers, particles not only impart their momentum to the fluid phase but also cause a slight displacement of water, which releases an acceleration wave that propagates away from the shoreline. Figure 11c suggests that for $Q < 0.5$, momentum transfers explain 25% to 50% of the wave amplitude, the rest being caused by the acceleration wave. For $Q > 5$, momentum transfers become the dominant mechanism of impulse wave formation. Naturally, in the absence of estimates of the effects of $S(t)$ and $Y(t)$ on impulse wave dynamics, this interpretation is a conjecture but an interesting lead to follow up on.

6.4. Implication of Weak Energy Conversion

The last point concerns the low-energy conversion factor f revealed in our experiments. Assuming equipartition between the kinetic and potential energies mentioned in section 5.3, we found that $f_{max} < 0.21$. Energy conversion factors were often higher in earlier experimental investigations: for *Kamphuis and Bowering* [1970], *Huber* [1980], and *Fritz and Hager* [2004], f fell in the 0.04–0.5 range; *Heller* [2007] found values as high as 0.85; whereas for submarine landslide-generated impulse waves, *Watts* [2000] found a narrow range of 0.02 to 0.13. A low f value indicates that in our experiments, most of the avalanche's kinetic energy was dissipated in the earliest moments after impact, which explains the smaller wave amplitude than for landslide-generated impulse waves. Another intriguing point was how little the wave train's energy was dependent on avalanche velocity. The key parameters controlling f were avalanche mass M_0 and water depth h. This may explain why we found the determination of the aggregated dimensionless number P_A for computing the wave amplitude to be so independent of Fr. This is an additional justification for the absence of Fr in the definition of the overall aggregated dimensionless number $\mathcal{R}$ used in Table 2.

6.5. Application to Avalanches

Contrary to landslide-induced impulse waves, there is no suitably well documented avalanche event which can serve as a test case. Much of the information available in the technical literature concerns run-up estimates of the impulse waves that overtopped slopes surrounding water basins. The only information about the amplitude of avalanche-generated impulse waves comes from the recent work by *Naaim* [2013], who combined numerical simulations with the experimental results compiled by *Kamphuis and Bowering* [1970]. He adjusted an empirical equation to the scaled wave amplitude sample

$$A' = Fr^{0.63}\left(0.18\exp(0.33\phi_0\Pi_3) - 0.30\exp(-14.28\phi_0\Pi_3)\right)\left(0.745 + 0.2\log\frac{\Pi_1}{\Pi_3}\right) \quad (34)$$

This equation holds for slide Froude numbers in the 0.5–3 range and for $\Pi_3 < 2.7$. Figure 16 shows that equation (34) roughly captures the experimental trend, with a coefficient of determination of $R^2 = 0.38$. The match is not perfect, but the simulations considerably simplified the avalanche's entry into the water basin (the avalanche was modeled as a fixed volume of fluid falling into a two-dimensional body of still water). The reasonable agreement between equation (34) and our data supports the idea that there is a lower bound in impulse wave amplitude.

7. Conclusion

In snow avalanche protection engineering, it is common practice to use empirical equations derived for landslides and rock avalanches to predict impulse wave features. However, the relative particle density of these gravity-driven flows is usually above 2500 kg m^{-3}, whereas snow avalanches are made of ice crystals whose density is slightly lower than that of water. An avalanche's bulk density is also typically low (in the 300–400 kg m^{-3} range). Snow avalanches are thus a special case in the family of gravity-driven flows. The present study aimed to determine whether snow avalanches cause the same effects as denser, gravity-driven flows striking a body of water. With this objective in mind, we explored two avenues for gaining insight into the impulse wave dynamics.

First, we developed a simple model based on mixture theory, which described the mass and momentum transfers between the particle and water phases within a fixed control volume. Scaling analysis demonstrated that the wave amplitude depended on eight dimensionless numbers (Re_p, Fr, Π_1 to Π_5, and θ). The dimension of the parameter space was thus too high for classic experimental investigation. We showed that it could be reduced by neglecting the influence of some dimensionless numbers (Re_p, Π_2, Π_4, Π_5), and aggregating the others into a single dimensionless product parameter $P = \Pi_1\Pi_3 Fr$ (or $Q = \Pi_1 Fr$ when working at constant Π_3). In this way, we ended up with approximate solutions for the wave amplitude A' in a two-parameter space: $A' = A'(Q, \theta)$. Comparison with experimental data showed that the model underestimated wave amplitudes at low Q values. For $Q < 0.5$, this suggested that momentum transfers at the particle scale would account for 25% to 50% of the wave amplitude, while the rest could be explained by the propagation of an acceleration wave that sets water in motion far from the impact zone. For $Q > 5$, the dominant mechanism of wave formation would be momentum transfer at the particle scale. This interpretation is speculative and deserves further investigation.

Second, we ran experiments using Froude similarity with a snow avalanche striking a water basin. Comparison with the data collected by *Heller and Hager* [2010] highlighted two important points. When plotting the wave features as a function of a single, aggregated dimensionless number such as $\mathcal{P}$ or P_A, we could not avoid a certain amount of noise in the data representation. In consequence, there was no unique way of aggregating the dimensionless numbers so as to reduce the dimension of the parameter space. To assess the power of prediction/explanation of the aggregated dimensionless numbers, we computed the coefficient of determination R^2, but due to the limited size of the data sets, there was no guarantee that this assessment was unbiased and unaffected by overfitting [*Harrell*, 2015]. A further point concerns the significant differences between our experimental data and those obtained by *Heller and Hager* [2010]. These differences probably result from the existence of two different initiation mechanisms for impulse waves generated by positively buoyant particle flows ($\Pi_3 < 1$). For $Fr > 2$ (for $\theta = 45°$), the avalanche forms a hydrodynamic impact crater in the impact zone, with part of the water volume lifting upward, then collapsing [*Fritz et al.*, 2003b; *Zweifel et al.*, 2006]. For $Fr < 2$, the avalanche penetrates into the water basin more progressively, without generating significant water uplift. The wave amplitude is much smaller in the latter case than in the former case. For this reason, we suggested that the wave amplitude in real-world cases is bounded by two limiting curves: experimental data collected by *Heller and Hager* [2010] provide the upper bound, while ours (and those obtained by *Kamphuis and Bowering* [1970]) provide the lower bound. Table 2 summarizes the different possibilities dependent on the choice of the aggregated dimensionless number $\mathcal{P}$ and $\mathcal{R}$.

Appendix A: Similarity

The *scale factor* between real scenarios and our setup was approximately $\lambda \sim 100$. For wet-snow avalanches, snow density approaches 400 kg m^{-3} [*Louge et al.*, 1997]; the snow is made of balls whose diameter usually ranges from 2–30 cm (mean diameter in the 7–12 cm range), with blocks as large as 50 cm [*Bartelt and McArdell*, 2009]. For dry-snow avalanches, the bulk density is usually lower (in the 200–300 kg m^{-3} range),

the grain size distribution is narrower, but the mean diameter is also close to 8 cm. The typical mean velocity ranges from 5 to 25 ms^{-1}, but velocities ranging from 25 to 50 ms^{-1} can be observed occasionally [*McClung and Schaerer*, 1993; *Ancey*, 2012, 2013].

In the experiments presented here, there was a partial geometric similarity with real-world scenarios. As a substitute for snow's properties, we used positively buoyant particles. There was a fairly good match between densities, but in our experiments, the particle size was larger by a factor of 10. This size distortion had the advantage of limiting any surface tension effects in our experiments, as the air cavities created by particles entering the water body were large. Surface tension effects can be estimated using the Weber number $We = \varrho_f u_p^2 d_p / \sigma_w$ (with $\sigma_w = 75 \times 10^{-3}$ N m^{-1}, the water surface tension at 0° C), which relates the particle kinetic energy to the surface energy. For snow avalanches, the magnitude of We is 5×10^5, whereas in our physical model, it was close to 300. In spite of the 3 orders of magnitude separating these figures, surface tension is negligibly small compared to inertial forces. Similar sized particle diameters would probably have introduced some undesired surface tension effects. Surface tension also affects wave propagation [*Johnson*, 1997], and its influence on wave dynamics can be assessed using a variant of the Weber number $We_w = \varrho_f g h^2 / \sigma_w$. For snow avalanches, this Weber number is huge ($We_w \sim 5 \times 10^8$), but for our experimental setup, it dropped to ~2500. For capillary-gravity waves, linear wave theory predicts that the phase speed C varies nonlinearly with the wave number $k = 2\pi/\Lambda$ (with Λ the wavelength)

$$C^2 = \frac{g}{k}\left(1 + \frac{k^2 h^2}{We_w}\right)\tanh(kh) \tag{A1}$$

This equation shows that the wavelength should be lower than $h We_w^{-1/2} \sim 3$ mm for surface tension to affect wave propagation. Our experiments had $\Lambda > 5h$, and from this perspective, wave propagation should be unaffected by surface tension. Yet in their impulse wave experiments at high Froude numbers, *Heller et al.* [2008] found out that for $We_w < 5000$ and flume Reynolds number $Re_f = \varrho_f \sqrt{g h^3}/\mu > 3 \times 10^5$, their data were substantially influenced by the scale effects resulting from surface tension and fluid viscosity.

The dynamic similarity criterion (based on the slide Froude number) was generally satisfied. For an avalanche entering a 20 m deep mountain lake at a velocity 20 ms^{-1}, the slide Froude number is $Fr \sim 1.4$. On average, in our experiments, granular avalanches entered into a 15 cm deep flume at a velocity of 1.7 ms^{-1}, which also led to a slide Froude number $Fr \sim 1.4$. As the initial experimental volume was small (typically $V_0 \sim 1$ L), the granular avalanche duration was short ($T_a \sim 1$ s). Froude similarity implies that this laboratory scenario corresponded to a snow avalanche duration of $\sqrt{\lambda} = 10$ s and snow volume of $\lambda^3 V_0 \sim 1000$ m^3. Although these figures are a factor of 10 to 100 lower than the typical values in real-world scenarios, they were consistent with the limitations of our experimental protocol explained in section 4.1. This constraint on avalanche duration did not cause a bias to the development of the impulse wave. Contrary to what can be observed with dense, high-speed flows ($\Pi_3 > 1$ and $Fr > 2$) [*Fritz et al.*, 2003b; *Zweifel et al.*, 2006], the maximum wave amplitude was observed shortly after the avalanche entered the water basin. For dense, high-speed flows, the impact generates a "hydrodynamic crater" and flow separation, and so there is a time lag between the avalanche entry and the occurrence of the wave's maximum amplitude.

A last remark concerns the ice cover on most lakes and reservoirs in high-altitude areas during the winter. Ice cover causes significant resistance to penetration and, in fact, small avalanches come to a halt on the snow-covered frozen surface. A 1 m thick ice cover has the bearing capacity in the order of 500 kPa [*Masterson*, 2009], and only large-volume or high-speed avalanches can exceed such strengths. Our investigation therefore neglected ice resistance.

Notation

Roman

- A_m maximum wave amplitude, m.
- B flume width, m.
- c drag coefficient.
- C phase speed, ms^{-1}.
- d_p particle diameter, m.
- E_a avalanche's kinetic energy, J.

E_k wave's kinetic energy, J.
E_w wave's total energy, J.
E_p wave's potential energy, J.
f energy conversion factor.
F correction factor.
Fr slide Froude number, $Fr = \bar{u}_0/\sqrt{gh}$.
g gravitational acceleration, ms^{-2}.
H_0 lock gate height, m.
h water depth, m.
H_m maximum wave height, m.
k wave number, m^{-1}.
ℓ_s chute length, m.
M_0 initial mass of particles, kg.
N number of particles in the control volume.
N_0 initial number of particles.
P, P_A, P aggregated dimensionless number.
$\mathcal{P}$ impulse product parameter $\mathcal{P} = Fr\,\Pi_2^{1/2}\Pi_1^{1/4}\cos^{1/2}(6\theta/7)$.
Q aggregated dimensionless number $Q = \Pi_1 Fr$.
$\mathcal{R}$ aggregated dimensionless number $\mathcal{R} = \Pi_1^{0.4}\Pi_2^{0.2}$.
R^2 coefficient of determination.
Re_p particle Reynolds number $Re_p = \varrho_f d_p \Delta u/\mu$.
s avalanche height, m.
s_0, s_{max} maximum avalanche height, m.
t time, s.
T_a duration of the avalanche, s.
$\bar{u}_0$ depth-averaged particle velocity, ms^{-1}.
u_f fluid velocity, ms^{-1}.
u_p particle velocity, ms^{-1}.
V_0 initial volume, m^3.
V control volume, m^3.
V_f volume of fluid, m^3.
We Weber number, We $= \varrho_f u_p^2 d_p/\sigma_w$.
x abscissa, m.
x_0 chute end, m.

Greek

α nonlinear regression parameter.
β nonlinear regression parameter.
γ nonlinear regression parameter.
η free-surface perturbation, m.
λ scale factor.
Λ wavelength, m.
ϕ solids fraction.
ϕ_0 solids fraction at the left boundary of the control volume.
Π_1 mass ratio, $\Pi_1 = M_0/(\varrho_f h^2 B)$.
Π_2 height ratio, $\Pi_2 = s_0/h$.
Π_3 density ratio, $\Pi_3 = \varrho_p/\varrho_f$.
Π_4 diameter-to-height ratio, $\Pi_4 = d_p/h$.
Π_5 diameter-to-width ratio, $\Pi_5 = d_p/B$.
σ_w water's surface tension, Nm^{-1}.
ϱ_f fluid density, kg m^{-3}.
ϱ_p particle density, kg m^{-3}.
ρ autocorrelation function.
θ chute inclination.
ϖ_p particle volume, m^3.

Acknowledgments
The present work was completed while Maurizio Brocchini was visiting the Laboratoire d'Hydraulique Environnementale, École Polytechnique Fédérale de Lausanne (EPFL). Christophe Ancey acknowledges the support of the EPFL Civil Engineering Department and the Swiss National Science Foundation (grant 200021_146271/1 for a project called "Physics of Basal Entrainment"). We are grateful to Valentin Heller for providing part of the experimental data [*Heller*, 2007; *Heller and Hager*, 2010]. We thank the editorial board and anonymous reviewers for the constructive comments that helped improve the initial manuscript. The preliminary tests were conducted by EPFL students: Pascal Venetz, Scott Favre, Christoph Perren, Robert Susset, and Isaac Thury. We are grateful to our colleagues Nicolas Andreini, Belinda Bates, and Bob de Graffenried for their help. Most data presented in this paper are available from an Excel spreadsheet in the supporting information (more information can be obtained upon request, from Christophe Ancey (christophe.ancey@epfl.ch) or Gianluca Zitti (g.zitti@univpm.it).

References

Ammann, W. J. (Ed.) (2000), *Der Lawinenwinter 1999*, Eidgenössisches Institut für Schnee- und Lawinenforschung, Davos.
Ancey, C. (2001), Dry granular flow down an inclined channel: Experimental investigations on the frictional-collisional regime, *Phys. Rev. E*, *65*, 11304.
Ancey, C. (2012), Gravity flow on steep slope, in *Buoyancy Driven Flows*, edited by E. Chassignet, C. Cenedese, and J. Verron, pp. 372–432, Cambridge Univ. Press, New York.
Ancey, C. (2013), Snow avalanches, in *Environmental Geomechanics*, edited by B. Schrefler and P. Delage, pp. 39–71, Wiley, New York.
Armanini, A., M. Larcher, E. Nucci, and M. Dumbser (2014), Submerged granular channel flows driven by gravity, *Adv. Water Resour.*, *63*, 1–10.
Bartelt, P., and B. W. McArdell (2009), Granulometric investigations of snow avalanches, *J. Glaciol.*, *55*, 829–833.
Berzi, D., and J. T. Jenkins (2008), A theoretical analysis of free-surface flows of granular-liquid mixtures, *J. Fluid Mech.*, *608*, 393–410.
Chadwick, P. (1999), *Continuum Mechanics: Precise Theory and Problems*, Dover, Mineola.
Cisse, M., E. W. Saw, M. Gibert, E. Bodenschatz, and J. Bec (2015), Turbulence attenuation by large neutrally buoyant particles, *Phys. Fluids*, *27*, 61702.
Couston, L. A., C. C. Mei, and M. R. Alam (2015), Landslide tsunamis in lakes, *J. Fluid Mech.*, *772*, 784–804.
Cremonesi, M., A. Frangi, and U. Perego (2011), A Lagrangian finite element approach for the simulation of water-waves induced by landslides, *Comput. Struct.*, *89*, 1086–1093.
Crosta, G. B., S. Imposimato, and D. Roddeman (2015), Granular flows on erodible and non erodible inclines, *Granul. Matter*, *17*, 667–685.
Di Risio, M., P. De Girolamo, G. Bellotti, A. Panizzo, F. Aristodemo, M. G. Molfetta, and A. F. Petrillo (2009), Landslide-generated tsunamis runup at the coast of a conical island: New physical model experiments, *J. Geophys. Res.*, *114*, C01009, doi:10.1029/2008JC004858.
Drew, D. A., and S. L. Passman (1999), *Theory of Multicomponent Fluids*, Springer, New York.
Evette, A., L. Peyras, H. François, and P. Mériaux (2011), Environmental risks and impacts of mountain reservoirs for artificial snow production in a context of climate change, *J. Alpine Res.*, *99*, doi:10.4000/rga.1481.
Fernández-Nieto, E. D., F. Bouchut, D. Bresch, M. J. Castro Díaz, and A. Mangeney (2008), A new Savage-Hutter type model for submarine avalanches and generated tsunami, *J. Comput. Phys.*, *227*, 7720–7754.
Frauenfelder, R., A. Jónsson, K. Lied, D. Schwerdtfeger, G. Bergum, Y. Bühler, and L. Stoffel (2014), Analysis of an artificially triggered avalanche at the Nepheline Syenite Mine on Stjernøya, Alta, Northern Norway, in *International Snow Science Workshop*, pp. 689–696, Montana State Univ., Banff.
Fritz, H. M., and W. H. Hager (2004), Near field characteristics of landslide generated impulse waves, *J. Waterw. Port Coast. Ocean Eng.*, *130*, 287–302.
Fritz, H. M., W. H. Hager, and H. E. Minor (2003a), Landslide generated impulse waves. 1. Instantaneous flow fields, *Exper. Fluids*, *35*, 505–519.
Fritz, H. M., W. H. Hager, and H. E. Minor (2003b), Landslide generated impulse waves. 2. Hydrodynamic impact crater, *Exper. Fluids*, *35*, 520–532.
Fuchs, H., M. Boes, and M. Pfister (2011), Impulse waves at Kühtai reservoir generated by avalanches and landslides, in *International Symposium on Dams and Reservoirs Under Changing Challenges*, pp. 701–708, CRC Press, Taylor and Francis Group, Boca Raton.
Gabl, R., J. Seibl, B. Gems, and M. Aufleger (2015), 3-D numerical approach to simulate the overtopping volume caused by an impulse wave comparable to avalanche impact in a reservoir, *Natl. Hazard Earth. Sys. Sci.*, *15*, 2617–2630.
Grilli, S. T., and P. Watts (2005), Tsunami generation by submarine mass failure. I: Modeling, experimental validation, and sensitivity analyses, *J. Waterway Port Coastal Ocean Eng.*, *131*, 283–297.
Guizien, K., and E. Barthélemy (2002), Accuracy of solitary wave generation by a piston wave maker, *J. Hydraul. Res.*, *40*, 321–330.
Harrell, F. E. (2015), *Regression Modeling Strategies — With Applications to Linear Models, Logistic and Ordinal Regression, and Survival Analysis, Springer Series in Statistics*, Springer, New York.
Heller, V. (2007), *Landslide Generated Impulse Waves: Prediction of Near-Field Characteristics*, PhD Thesis, ETHZ, Zürich, Switzerland.
Heller, V. (2011), Scale effects in physical hydraulic engineering models, *J. Hydraul. Res.*, *49*, 293–306.
Heller, V., and W. H. Hager (2010), Impulse product parameter in landslide generated impulse waves, *J. Waterway Port Coastal Ocean Eng.*, *136*, 145–155.
Heller, V., and W. H. Hager (2011), Wave types of landslide generated impulse waves, *Ocean Eng.*, *38*, 630–640.
Heller, V., and W. H. Hager (2014), A universal parameter to predict subaerial landslide tsunamis?, *J. Marine Sci. Eng.*, *2*, 400–412.
Heller, V., and J. Spinneken (2013), Improved landslide-tsunami prediction: Effects of block model parameters and slide model, *J. Geophys. Res.*, *118*, 1489–1507.
Heller, V., and J. Spinneken (2015), On the effect of the water body geometry on landslide-tsunamis: Physical insight from laboratory tests and 2D to 3D wave parameter transformation, *Cost. Eng.*, *104*, 113–134.
Heller, V., W. H. Hager, and H. E. Minor (2008), Scale effects in subaerial landslide generated impulse waves, *Exper. Fluids*, *44*, 691–703.
Heller, V., W. H. Hager, and H. E. Minor (2009), Landslide generated impulse waves in reservoirs — Basics and computation, in *VAW Mitteilung 211*, Versuchsanstalt für Wasserbau, Hydrologie und Glaziologie, VAW, ETH Zürich, Zürich, Switzerland.
Holyoake, A. J., and J. N. McElwaine (2012), High-speed granular chute flows, *J. Fluid Mech.*, *710*, 35–71.
Hsu, T. J., J. T. Jenkins, and P. L. F. Liu (2004), On two-phase sediment transport: Sheet flows of massive particles, *Proc. R. Soc. A*, *460*, 2223–2250.
Huber, A. (1980), *Schwallwellen in Seen aus Folge von Felsstürzen*, VAW, Eidg. Tech. Hochsch, Zürich, Switzerland.
Huber, A., and W. H. Hager (1997), Forecasting impulse waves in reservoirs, in *19ème Congrès des Grands Barrages, chap. 31*, pp. 993–1005, ICOLD, Paris, Florence.
Iverson, R. M. (2005), Debris-flow mechanics, in *Debris-flow hazards and related phenomena*, edited by M. Jakob and O. Hungr, pp. 105–134, Springer, Berlin.
James, N., S. Boyaval, A. Caboussat, and M. Picasso (2014), Numerical simulation of 3D free surface flows, with multiple incompressible immiscible phases. Applications to impulse waves, *Int. J. Numer. Meth. Fluids*, *76*, 1004–1024.
Johnson, R. S. (1997), *A Modern Introduction to the Mathematical Theory of Water Waves*, Cambridge Univ. Press, Cambridge, U. K.
Kamphuis, J. W., and R. J. Bowering (1970), Impulse waves generated by landslides, in *12th Conference on Coastal Engineering*, vol. 1, edited by J. W. Johnson, pp. 575–586, ASCE, New York, and Washington, D. C.
Kelfoun, K., T. Giachetti, and P. Labazuy (2010), Landslide-generated tsunamis at Réunion Island, *J. Geophys. Res.*, *115*, F04012, doi:10.1029/2009JF001381.
Lhuillier, D., C. H. Chang, and T. G. Theofanous (2013), On the quest for a hyperbolic effective-field model of disperse flows, *J. Fluid Mech.*, *731*, 184–194.
Louge, M. Y., R. Steiner, S. C. Keast, R. Decker, J. Dent, and M. Schneebeli (1997), Application of capacitance instrumentation to the measurement of density and velocity of flowing snow, *Cold Reg. Sci. Technol.*, *25*, 47–63.

Louge, M. Y., A. Valance, P. Lancelot, R. Delannay, and O. Artieres (2015), Granular flows on a dissipative base, *Phys. Rev. E*, *92*, 22204.
Løvholt, F., G. Pedersen, C. B. Harbitz, S. Glimsdal, and J. Kim (2015), On the characteristics of landslide tsunamis, *Philos. Trans. R. Soc. A*, *373*, 20140376.
Masterson, D. M. (2009), State of the art of ice bearing capacity and ice construction, *Cold Reg. Sci. Technol.*, *58*, 99–112.
Mathai, V., V. N. Prakash, J. Brons, C. Sun, and D. Lohse (2015), Wake-driven dynamics of finite-sized buoyant spheres in turbulence, *Phys. Rev. Lett.*, *115*, 124501.
McClung, D. M., and P. A. Schaerer (1993), *The Avalanche Handbook*, The Mountaineers, Seattle, Wash.
McTigue, D. F. (1981), Mixture theory for suspended sediment transport, *J. Hydraul. Eng.*, *107*, 659–673.
Meruane, C., A. Tamburrino, and O. Roche (2010), On the role of the ambient fluid on gravitational granular flow dynamics, *J. Fluid Mech.*, *648*, 381–404.
Mohammed, F., and H. M. Fritz (2012), Physical modeling of tsunamis generated by three-dimensional deformable granular landslides, *J. Geophys. Res.*, *117*, C11015, doi:10.1029/2011JC007850.
Naaim, M. (2013), Impulse water waves generated by snow avalanches, in *International Snow Science Workshop*, pp. 619–624, Montana State Univ., Grenoble, France.
Nishimura, K., S. Keller, J. McElwaine, and Y. Nohguchi (1998), Ping-pong ball avalanche at a ski jump, *Granul. Matter*, *1*, 51–56.
Noda, E. (1970), Water waves generated by landslides, *J. Waterway Harb. Coast. Eng. Div. ASCE*, *96*, 835–855.
Ouriemi, M., P. Aussillous, and E. Guazzelli (2009), Sediment dynamics. Part 1. Bed-load transport by laminar shearing flows, *J. Fluid Mech.*, *636*, 295–319.
Pailha, M., and O. Pouliquen (2009), A two-phase flow description of the initiation of underwater granular avalanches, *J. Fluid Mech.*, *633*, 115–135.
Panizzo, A., P. De Girolamo, and A. Petaccia (2005), Forecasting impulse wave generated by subaerial landslides, *J. Geophys. Res.*, *110*, C12025, doi:10.1029/2004JC002778.
Pudasaini, S. P. (2014), Dynamics of submarine debris flow and tsunami, *Acta Mech.*, *225*, 2423–2434.
Quecedo, M., and M. Pastor (2004), Numerical modelling of impulse wave generated by fast landslides, *Int. J. Numer. Meth. Engng.*, *59*, 1633–1656.
Revil-Baudard, T., and J. Chauchat (2013), A two-phase model for sheet flow regime based on dense granular flow rheology, *J. Geophys. Res. Oceans*, *118*, 619–634, doi:10.1029/2012JC008306.
Savage, S. B., and K. Hutter (1989), The motion of a finite mass of granular material down a rough incline, *J. Fluid Mech.*, *199*, 177–215.
Serrano-Pacheco, A., J. Murillo, and P. García-Navarro (2009), A finite volume method for the simulation of the waves generated by landslides, *J. Hydrol.*, *373*, 273–289.
Slingerland, R. L., and B. Voight (1979), Occurrences, properties, and predictive models of landslide-generated water waves, in *Rockslides and Avalanches*, vol. 2, edited by B. Voight, pp. 317–397, Elsevier, Amsterdam.
Truesdell, C. (1984), *Rational Thermodynamics*, 2nd ed., Springer Verlag, New York.
Truscott, T. T., B. P. Epps, and A. H. Techet (2012), Unsteady forces on spheres during free-surface water entry, *J. Fluid Mech.*, *704*, 173–210.
Truscott, T. T., B. P. Epps, and J. Belden (2014), Water entry of projectiles, *Annu. Rev. Fluid Mech.*, *46*, 355–378.
Turnbull, B., and J. McElwaine (2008), Experiments on the non-Boussinesq flow of self-igniting suspension currents on a steep open slope, *J. Geophys. Res.*, *113*, F01003, doi:10.1029/2007JF000753.
Vischer, D. L., and W. H. Hager (1998), *Dam Hydraulics*, Wiley, Chichester, U. K.
Walder, J. S., P. Watts, O. E. Sorensen, and K. Jansse (2003), Tsunamis generated by subaerial mass flows, *J. Geophys. Res.*, *108*, B2563, doi:10.1029/2001JB000707.
Watts, P. (2000), Tsunami features of solid block underwater landslides, *J. Waterway Port Coastal Ocean Eng.*, *126*, 144–152.
White, F. M. (2011), *Fluid Mechanics*, McGraw-Hill, New York.
Whitham, G. B. (1974), *Linear and Nonlinear Waves*, Wiley, New York.
Zweifel, A., W. H. Hager, and H. E. Minor (2006), Plane impulse waves in reservoirs, *J. Waterway Port Coastal Ocean Eng.*, *132*, 358–368.